iScience

Article

# Bat RNA viruses employ viral RHIMs orchestrating species-specific cell death programs linked to Z-RNA sensing and ZBP1-RIPK3 signaling

## Graphical abstract

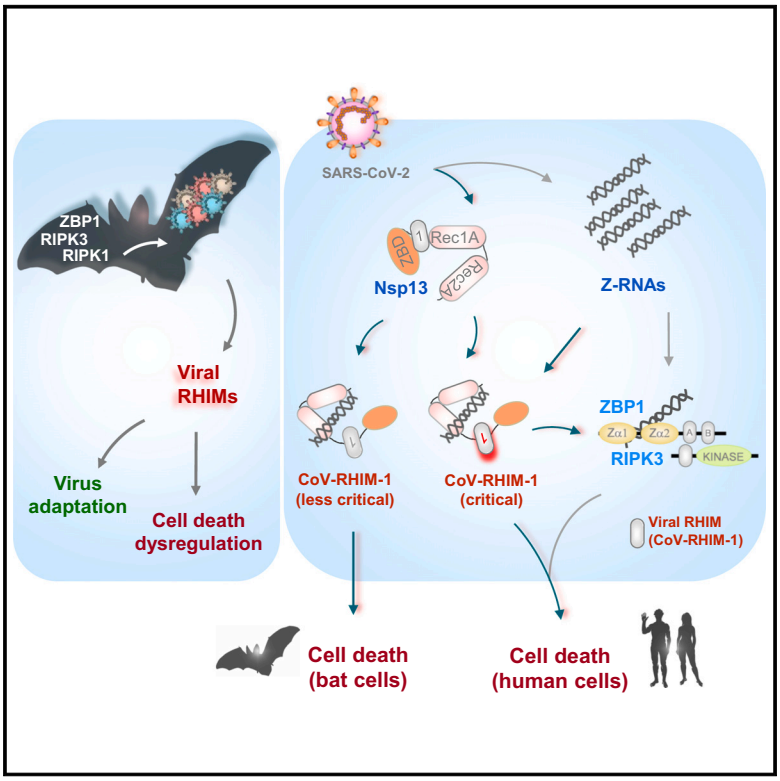


## Authors

Sanchita Mishra, Disha Jain, Ayushi Amin Dey, ..., Shashank Tripathi, Mahipal Ganji, Sannula Kesavardhana

## Correspondence

skesav@iisc.ac.in

## In brief

Molecular biology; Immunology; Cell biology

## Highlights

- RNA viruses operate viral RHIMs in promoting human and bat-specific cell death
- SARS-CoV-2 Nsp13 promotes host cell death with its viral RHIM and RNA-binding channel
- SARS-CoV-2 Nsp13 promotes higher-order ZBP1 and RIPK3 complex assembly and cell death
- SARS-CoV-2 genome consists of bonafide Z-RNAs which promote Nsp13-mediated cell death

Mishra et al., 2024, iScience *27*, 111444
December 20, 2024 
https://doi.org/10.1016/j.isci.2024.111444

CellPress

iScience

CellPress
OPEN ACCESS

Article

# Bat RNA viruses employ viral RHIMs orchestrating species-specific cell death programs linked to Z-RNA sensing and ZBP1-RIPK3 signaling

Sanchita Mishra,[1] Disha Jain,[1,4] Ayushi Amin Dey,[1,4] Sahana Nagaraja,[1,4] Mansi Srivastava,[1] Oyahida Khatun,[2,3] Keerthana Balamurugan,[1] Micky Anand,[1] Avinash Karkada Ashok,[1] Shashank Tripathi,[2,3] Mahipal Ganji,[1] and Sannula Kesavardhana[1,5,*]

[1]Department of Biochemistry, Division of Biological Sciences, Indian Institute of Science, Bengaluru, Karnataka 560012, India
[2]Department of Microbiology and Cell Biology, Division of Biological Sciences, Indian Institute of Science, Bengaluru 560012, India
[3]Centre for Infectious Disease Research, Indian Institute of Science, Bengaluru 560012, India
[4]These authors contributed equally
[5]Lead contact
*Correspondence: skesav@iisc.ac.in
https://doi.org/10.1016/j.isci.2024.111444

## SUMMARY

RHIM is a protein motif facilitating the assembly of large signaling complexes triggering regulated cell death. A few DNA viruses employ viral RHIMs mimicking host RHIMs and counteract cell death by interacting with host RHIM-proteins to alleviate antiviral defenses. Whether RNA viruses operate such viral RHIMs remains unknown. Here, we identified viral RHIMs in Nsp13 of SARS-CoV-2 and other bat RNA viruses, providing the basis for bats as the hosts for their evolution. Nsp13 promoted viral RHIM and RNA-binding channel-dependent cell death. However, Nsp13 viral RHIM is more critical for human cell death than in bat-derived Tb1 Lu cells, suggesting species-specific regulation. Nsp13 showed RHIM-dependent interactions with ZBP1 and RIPK3, forming large complexes and promoting ZBP1-RIPK3 signaling-mediated cell death. Intriguingly, the SARS-CoV-2 genome consisted of Z-RNA-forming segments promoting Nsp13-dependent cell death. Our findings reveal the functional viral RHIMs of bat-originated RNA viruses regulating host cell death associated with ZBP1-RIPK3 signaling, indicating possible mechanisms of cellular damage and cytokine storm in bat-originated RNA virus infections.

## INTRODUCTION

Pathogenic RNA virus infections often result in uncontrolled tissue damage and inflammatory responses, which prime disease pathogenesis.[1–3] Severe acute respiratory syndrome coronavirus 2 (SARS-CoV-2) is associated with mild to severe respiratory infections and causes coronavirus disease 2019 (COVID-19).[4,5] COVID-19 patients develop pneumonia and acute respiratory distress syndrome (ARDS), which lead to the failure of respiratory function.[1,4,5] However, the host and viral mechanisms underlying disease pathogenesis in COVID-19 and other human respiratory infections are unclear. Aberrant cell death and cytokine storm have been reported to be associated with COVID-19 pathogenesis.[1,2,6] RNA viruses, including CoVs, are adapted to evade host defense responses to promote their spread and pathogenesis in the infected hosts.[7,8] Also, these RNA viruses show restricted type I interferon (IFN) production and cause dysregulated immune and proinflammatory responses in the lung.[1,8,9]

Regulated inflammatory cell death is an innate host defense response to virus infections.[3,10,11] Inflammatory cell death removes the viral replication niche by eliminating the virus-infected cells and mounts protective immune responses and repair processes.[1,9] Type I IFNs promote inflammatory cell death as a protective host defense mechanism during viral infections.[9,12] Human receptor-interacting serine/threonine protein kinase 1 (RIPK1), RIPK3, Toll/IL-1 receptor domain-containing adapter protein-inducing IFN-β (TRIF), and Z-nucleic acid binding protein 1 (ZBP1) are inflammatory cell death signaling proteins.[13,14] These proteins have a conserved receptor-interacting protein (RIP)-homotypic interaction motif (RHIM), which confers protein-protein interactions of these cell death proteins. RHIM-mediated protein-protein interactions trigger the formation of higher-order signaling complexes, structurally resembling an amyloid fibrillar assembly, which promote cell death and inflammation.[14–16] The RIPK3 in this complex mediates the activation of mixed lineage kinase domain-like (MLKL), leading to the execution of an inflammatory form of cell death necroptosis.[15,17,18] The RIPK3 also promotes RHIM-dependent recruitment of RIPK1 and activation of caspase-8-dependent apoptosis.[10,18,19] Necroptosis is essential for eliminating virus-infected cells and blocking viral spread, but its dysregulation sometimes aggravates inflammation and tissue damage.[3,9–11] RIPK3 and ZBP1 are the key triggers of necroptosis during viral infections.[19–27] These proteins are also associated

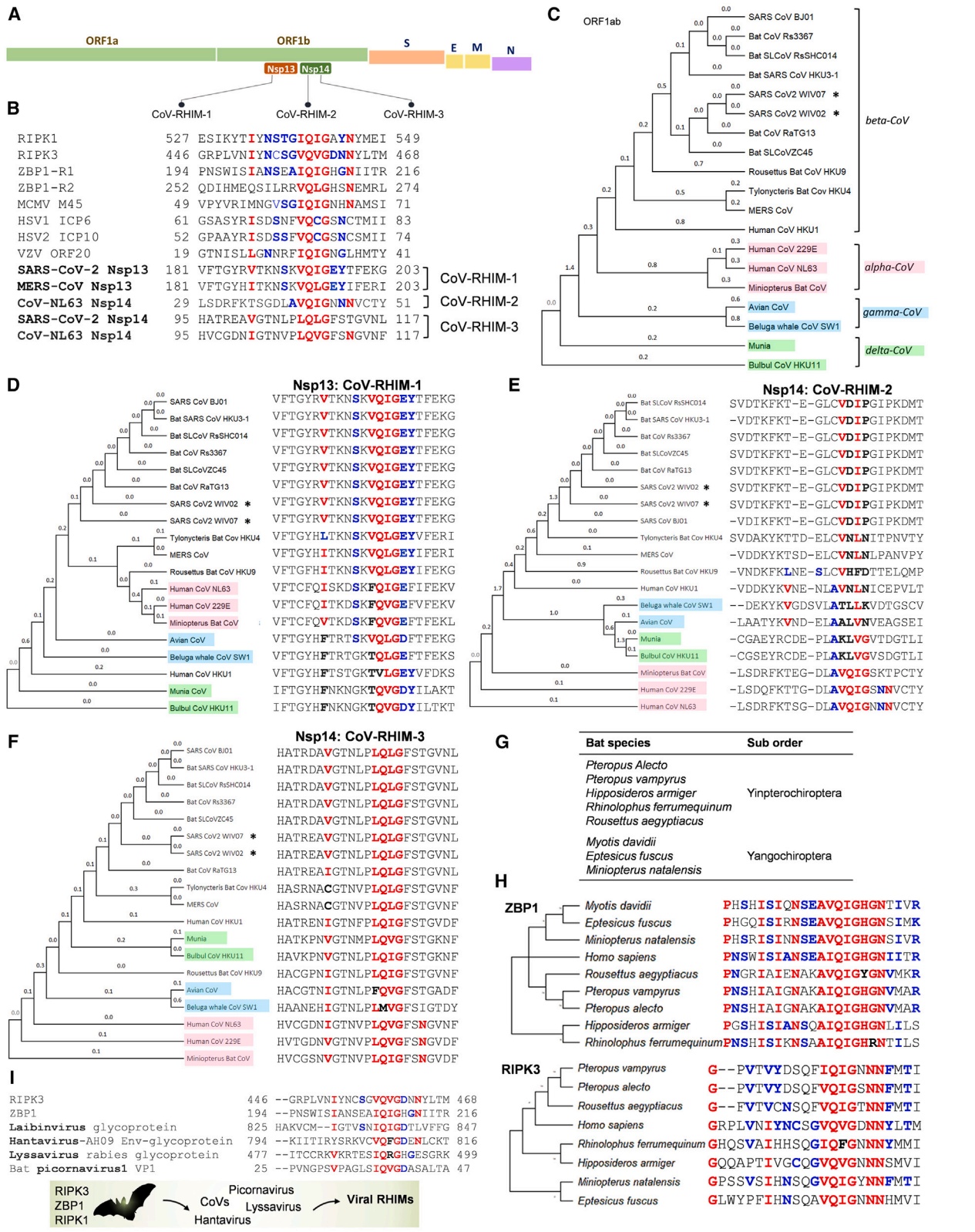


*(legend on next page)*

with activating inflammasome-driven pyroptosis, and a multifaceted cell death modality called PANoptosis.[6,10,28,29] ZBP1 is an innate immune sensor recognizing viral Z-RNAs generated during viral replication.[3,10,30] Upon ZBP1 activation, RHIM-mediated interaction of ZBP1 and RIPK3 triggers cell death and inflammation. Due to the critical role of RHIMs in driving ZBP1-RIPK3 signaling and antiviral host defense, a few DNA viruses (herpesviruses) have evolved to mimic host RHIMs to counteract ZBP1-RIPK3 signaling.[20,24,31] These viral RHIMs bind to host RIPK3 to restrict its interaction with RIPK1 and ZBP1 and the formation of cell death signaling complexes to help continue viral replication and spread.[20,21,24,26,31–33] Interestingly, viral RHIMs of HSV-1 restrict RIPK3-mediated cell death in human cells, which is a natural host species, but promote cell death in mouse cells, suggesting the species-specific functions of viral RHIMs in either promoting or restricting cell death activation.[24,31,34] Recent studies show that poxvirus vaccinia encodes Z-RNA competitors of ZBP1 activation to regulate ZBP1-RIPK3 signaling.[35,36] Unlike DNA viruses, influenza viruses do not encode any RHIM-mediated suppressors but instead activate ZBP1-RIPK3-dependent cell death with inflammatory damage.[1,3,10] Also, aberrant cell death, inflammation, and necrotic lung damage are the clinical signs observed during pathogenic influenza and SARS-CoV-2 infections.[1,6,28,37,38] This indicates a possible lack of viral RHIMs or the presence of cell death-promoting viral RHIMs in pathogenic respiratory viruses. However, whether RNA viruses operate viral RHIMs to modulate host cell death responses is unknown.

Here, we report the identification of viral RHIMs of CoVs (CoV-RHIMs) in Nsp13 and Nsp14 proteins. CoV-RHIM in Nsp13 of pathogenic CoVs (SARS-CoV, MERS-CoV, and SARS-CoV-2) is highly conserved and retains RHIM-like features compared to other human CoVs, whereas CoV-RHIMs in Nsp14 were conserved in less pathogenic human CoVs. Also, our observations indicate bat RHIM-proteins in driving the evolution of viral RHIMs in RNA viruses. Unlike RHIM proteins of DNA viruses, CoV-RHIM of SARS-CoV-2 Nsp13 promoted cell death and the RNA binding channel of Nsp13 is critical for this function. Intriguingly, Nsp13 showed species-specific distinct mechanisms of cell death regulation. Also, SARS-CoV-2 Nsp13 formed RHIM-dependent complexes with the ZBP1 and promoted the formation of ZBP1 and RIPK3 higher-order complexes. Further biochemical studies suggest the role of SARS-CoV-2 Z-RNAs in promoting Nsp13-mediated cell death. Our observations demonstrate the evolution and operation of viral RHIMs in RNA viruses that might be linked to cellular damage and cytokine storm.

## RESULTS

### Identification of viral RHIMs in SARS-CoV-2 Nsp13 and Nsp14 proteins

RHIMs consist of core tetrad (**I/V-Q-I/V/L/C-G**) residues promoting the stacking of β-sheet structures and formation of amyloid-like higher-order signaling complexes.[14,15,32,39,40] Mutating these core tetrad residues inhibits the higher-order structure formation, cell death signaling, and inflammation.[15,20,21,23,32,33,41,42] We sought to identify the viral RHIM-like sequences in SARS-CoV-2 and other CoVs by protein sequence and structure-based analysis. Interestingly, we identified three RHIM-like sequences in Nsp13 (RNA helicase) and Nsp14 (exoribonuclease) of the SARS-CoV-2 and other CoVs (Figures 1A and 1B). These RHIM-like CoV sequences (called CoV-RHIMs hereafter) were conserved in all the SARS-CoV-2 variants and attained β-sheet conformation in crystal structures of Nsp13 and Nsp14 proteins and are surface accessible (Figure S1A).[43,44] The core tetrad in CoV-RHIM-1 and -3 of the SARS-CoV-2 showed high similarity with other viral and host RHIM-proteins, although the CoV-RHIM-2 was mutated in its core tetrad residues (Figures 1B and 1D–1F). In addition, a conserved Val/Ile (V/I) upstream of the core tetrad was noticeable in SARS-CoV-2 RHIM-proteins like established RHIM-proteins (Figure 1B). These observations suggest that Nsp13 and Nsp14 of SARS-CoV-2 show RHIM-like features and indicate their potential role in modulating host cell death and inflammatory responses.

Our further analysis of bat-originated beta-CoVs and other CoVs showed notable differences and distinct evolutionary patterns (Figures 1C–1F).[4,45] The CoV-RHIM-1 in Nsp13 was conserved in human and bat beta-CoVs, including Bat-CoV RaTG13, which is one of the closest associates of SARS-CoV-2, suggesting the occurrence of CoV-RHIMs in bat-originated CoVs (Figure 1D). HKU1, a beta-CoV causing mild respiratory illness in humans, showed variation in the CoV-RHIM-1 and was distantly related to the pathogenic beta-CoVs in phylogenetic analysis (Figures 1C and 1D). Human-CoV 229E and NL63 are alpha-CoVs causing mild respiratory symptoms like HKU1.[46] These CoVs also had a mutation at the first position of the core tetrad (V/I→F) (Figure 1D). These observations further suggested an intriguing variation in CoV-RHIM-1 of the human CoVs that distinguishes mild and severe human CoV infections. We identified two additional CoV-RHIMs in Nsp14

**Figure 1. Identification of CoV-RHIMs in Nsp13 and Nsp14 of SARS-CoV-2 and bats as hosts in viral RHIM evolution in RNA viruses**

(A) Schematic representation showing the genomic organization of SARS-CoV-2 and CoV-RHIMs in Nsp13 and Nsp14 proteins encoded by ORF1b.

(B) Amino acid residues and their relative conservation in RHIMs of human proteins (RIPK1, RIPK3, and ZBP1), M45 of murine cytomegalovirus (MCMV), ICP6 and ICP10 of herpes simplex virus (HSV), ORF20 of varicella-zoster virus (VZV) and Nsp13 and Nsp14 of CoVs (SARS-CoV-2, MERS-CoV and CoV-NL63). Human ZBP1 consists of two RHIM sequences (ZBP1-R1 and ZBP1-R2).

(C) Phylogenetic tree representing the relatedness of different CoV genera based on protein sequences encoded by ORF1ab.

(D–F) The phylogenetic tree and the relative conservation of CoV-RHIM-1 in Nsp13 (D), CoV-RHIM-2 (E), and CoV-RHIM-3 (F) in Nsp14 across CoVs.

(G) Bat species from Yangochiroptera and Yinpterochiroptera suborders considered for analyzing bat-originated RIPK3 and ZBP1 protein sequences.

(H) Protein sequence alignment and phylogenetic trees showing relative conservation of human and bat RHIM-sequences within RIPK3 and ZBP1 proteins.

(I) The potential viral RHIM signatures in lyssavirus rabies, picornavirus, and hantaviruses that originate from bats. The core tetrad residues and the proximal conserved residues of RHIMs are highlighted in bold; conserved or identical residue positions in RHIM sequences are highlighted in red; less conserved but chemically similar residue positions in RHIM sequences are highlighted in blue. Asterisk (*) symbols indicate Wuhan SARS-CoV-2 isolates.

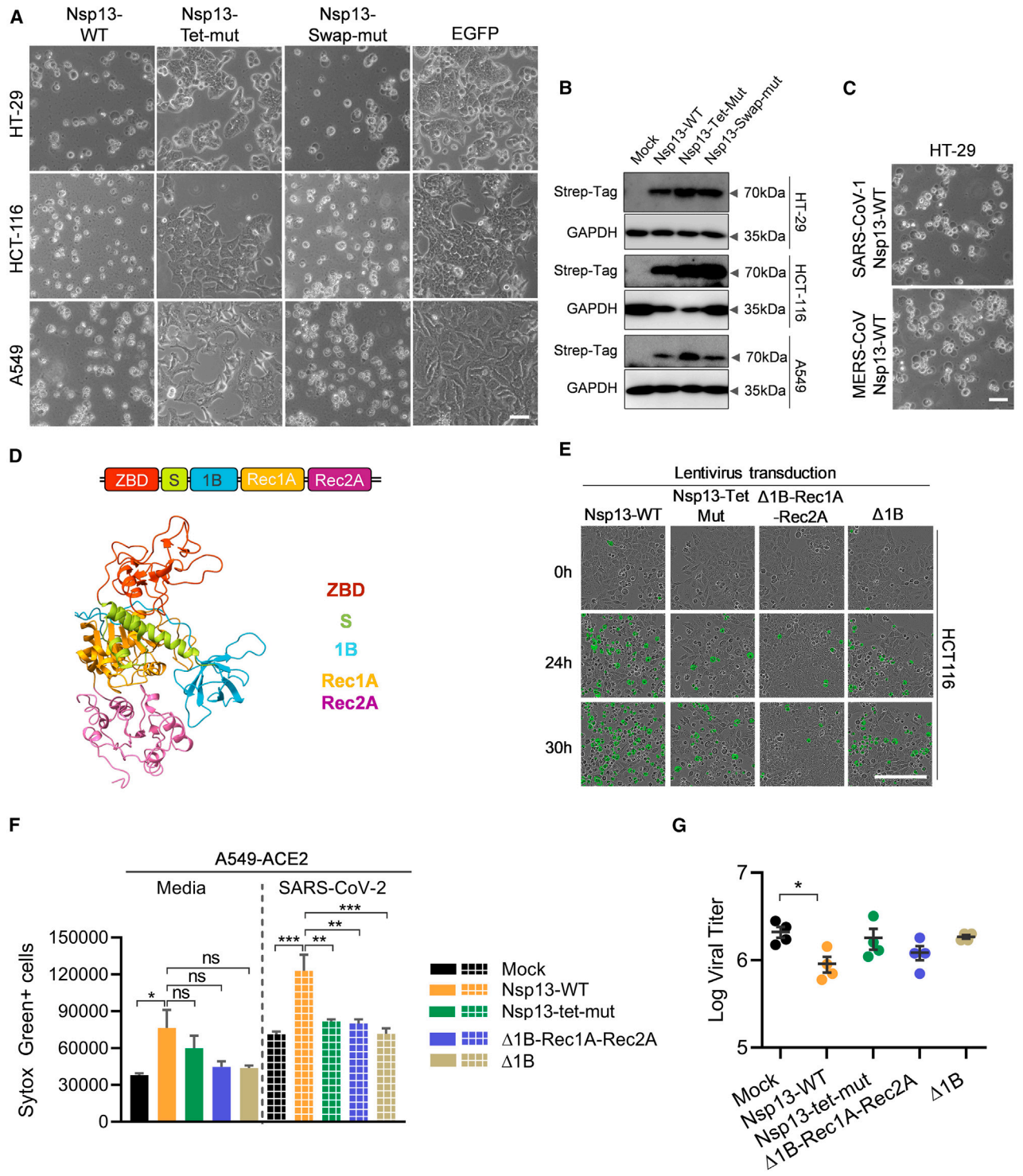


**Figure 2. Nsp13 of pathogenic beta-CoVs promotes cell death in human cells and is dependent on CoV-RHIM-1 and RNA-binding channel**

(A) Microscopic analysis of HT-29, HCT-116, and A549 cells infected with lentiviruses expressing SARS-CoV-2 Nsp13-WT, Nsp13-Tet-mut, Nsp13-Swap-mut and EGFP followed by puromycin treatment. Scale bar, 50μm.

(B) Immunoblot analysis of lysates from HT-29, HCT-116, and A549 cells showing expression of Nsp13-WT, Nsp13-Tet-mut, Nsp13-Swap-mut (Strep-Tag) and GAPDH after lentivirus transduction.

(C) Microscopic analysis of HT-29 cells transduced with lentiviruses expressing SARS-CoV-1 and MERS-CoV Nsp13-WT. Scale bar, 50μm.

(D) The annotation of domains in the Nsp13 structure (PDB ID: 6ZSL).

*(legend continued on next page)*

and Gln (Q) and Gly (G) at positions 2 and 4 of the core tetrad in CoV-RHIM-2 are mutated in pathogenic beta-CoVs (Figures 1E and 1F). Unlike beta-CoVs, the alpha-CoVs (229E and NL63) consisted of the conserved residues promoting RHIM-mediated complex formation (Figure 1E). Thus, the CoV-RHIMs show variations between alpha and beta-CoVs, which were zoonotically transmitted to humans but diverged in their pathogenicity. The CoV-RHIM-3 in Nsp14 is highly conserved across CoVs, except in gamma-CoVs. In addition, CoV-RHIM-3 of alpha-CoVs showed high similarity to human-RHIMs. These observations suggest that SARS-CoV-2 and other CoV proteins show RHIM-like features and indicate their potential role in modulating host cell death and inflammatory responses.

Why CoVs consist of multiple RHIM-like sequences in nonstructural proteins, and what factors drove the evolution of viral RHIMs in CoVs? Bats are the primary reservoirs of CoVs and identifying bat CoV-RaTG13 and other related viruses as the closest relative of the SARS-CoV-2 further elucidated the association of bat CoVs with severe human infections.[4,6,45,47] Also, bats are the natural reservoirs for other pathogenic RNA viruses that trigger cellular damage and inflammatory responses.[6,47] Bats are mammals with immune gene networks like humans.[48–50] Bats also express RIPK3 and ZBP1, which are the potential targets for viral RHIM-mediated host modulation.[51,52] We observed that the core tetrad and surrounding residues in the RHIMs of bat RIPK3 and ZBP1 are conserved in both Yangochiroptera and Yinpterochiroptera suborders and are nearly identical to the RHIMs of human RIPK3 and ZBP1 (Figures 1G and 1H). This raises the possibility that CoVs might have encountered the antiviral effects of bat RIPK3 and ZBP1 prior to their zoonotic transfer into humans. This suggests that zoonotic RNA viruses originating in bats might evolve to operate viral RHIMs. In line with this hypothesis, we found that lyssavirus rabies, picornavirus, and hantaviruses originated from bats encode RHIM-like sequences (Figure 1I). These observations thus suggest the likely evolution of viral RHIM-like sequences in bat RNA viruses. When the bat RNA viruses infect humans, they may either counteract or promote human RHIM-mediated cell death, contributing to virus propagation and severe pathology.

## CoV-RHIM-1 of 1B domain and RNA binding channel promote Nsp13-mediated cell death

To examine whether CoV-RHIMs are associated with cell death regulation in human cells, we generated lentiviruses expressing SARS-CoV-2 Nsp13-WT. We noticed robust cell death in HT-29 cells transduced with Nsp13-expressing lentiviruses but not EGFP-expressing lentiviruses, followed by puromycin selection (Figure 2A). The detection of Nsp13 protein expression in HT-29 cells indicated that the cell death was not due to defective Nsp13 lentiviruses (Figure 2B). A549 and HCT116 cells also showed robust cell death after Nsp13-lentivirus transduction (Figures 2A and 2B). This suggests that SARS-CoV-2 Nsp13 expression promotes cell death in multiple human cell types. We also observed robust cell death in HT-29 cells transduced with SARS-CoV-1 and MERS-CoV Nsp13 lentiviruses (Figure 2C). SARS-CoV-2 Nsp13 consists of two RecA ATPase domains (Rec1A and Rec2A), which unwind DNA and RNA.[53,54] This helicase activity of Nsp13 is critical for the progressive elongation of the RNA-dependent RNA polymerase (RdRp) on a highly structured SARS-CoV-2 RNA genome.[53–55] Nsp13 also consists of a Zinc-binding domain (ZBD), a stalk region (S), and an inserted domain 1B (hereafter called 1B) (Figure 2D). Rec1A, Rec2A, 1B, and a part of the S domain of the Nsp13 form an RNA binding channel, and the CoV-RHIM-1 spans to domain 1B (Figure 2D).[53–55] To understand how Nsp13 induces cell death, we generated strategic domain deletion constructs of the Nsp13, and immunoblotting analysis confirmed their expression at the protein level (Figures S1B and S1C). Deletion of 1B, Rec1A, and Rec2A or only Rec1A and Rec2A showed significant inhibition of Nsp13-mediated cell death (Figure S1D). This suggested the critical role of 1B, Rec1A, and Rec2A in Nsp13-dependent cell death. In addition, deletion of the ZBD or 1B domain did not diminish Nsp13-mediated cell death (Figure S1D). Interestingly, deletion of 1B and ZBD-S domains showed diminished Nsp13-mediated cell death (Figure S1D). These observations indicate that 1B domain deletion in combination with Rec1A-Rec2A or ZBD-S domains abolished Nsp13-dependent cell death. Thus, Nsp13-dependent cell death in human cells requires an RNA binding channel (formed by Rec1A, Rec2A, 1B, and a part of S) function.

To further understand the role of CoV-RHIM-1 in Nsp13-mediated cell death, we mutated the core tetrad residues of the CoV-RHIM-1 to alanine (VQIG→AAAA, named Nsp13-Tet-mut). We also swapped the CoV-RHIM-1 core tetrad of the SARS-CoV-2 Nsp13 with less pathogenic HKU1-CoV residues (VQIG→TVLG, named Nsp13-Swap-mut). Nsp13-Tet-mut lentiviruses did not promote cell death in HT-29, A549, and HCT-116 cells, but Nsp13-Swap-mut induced cell death similarly to Nsp13-WT (Figures 2A and 2B). This implies that CoV-RHIM-1 is critical for Nsp13-mediated cell death in human cells. Nsp13-Swap-mut did not affect Nsp13-mediated cell death, perhaps due to conserved CoV-RHIM-1 conformation. Also, real-time monitoring of cell death using sytox green staining in HCT-116 cells transduced or transiently transfected with Nsp13 constructs showed reduced cell death when disrupting RNA binding channel or mutating CoV-RHIM-1 (Figures 2E, S1E, and S1G). We also observed reduced apoptosis in HCT-116 cells when CoV-RHIM-1 was mutated, or the RNA-binding channel was

(E) Representative Sytox green staining images of HCT-116 cells infected with lentiviruses expressing SARS-CoV-2 Nsp13-WT, Nsp13-Tet-mut, Nsp13-Δ1B and Nsp13- Δ1B-Rec1A-Rec2A acquired by Incucyte imaging analysis system. Scale bar, 200μm.
(F) Cell death levels in mock or SARS-CoV-2 infected A549-ACE2 cells ectopically expressing Nsp13 constructs as indicated. Cell death was monitored by Sytox green staining at 48 h of infection. ***$p$ = 0.0002 (comparison of SARS-CoV-2 infected mock and Nsp13-WT cells), ***$p$ = 0.0003 (comparison of SARS-CoV-2 infected Nsp13-WT and Δ1B expressing cells), **$p$ = 0.0076 (comparison of SARS-CoV-2 infected Nsp13-WT and Nsp13-Tet-mut expressing cells),**$p$ = 0.0043 (comparison of SARS-CoV-2 infected Nsp13-WT and Δ1B-Rec1A-Rec2A expressing cells), *$p$ = 0.0178, ns – not significant (one way ANOVA).
(G) SARS-CoV-2 infectivity titers in cell supernatants of mock or SARS-CoV-2 infected A549-ACE2 cells ectopically expressing Nsp13 constructs, measured by plaque assay. *$p$ = 0.0318 (one way ANOVA). Data shown are mean ± SEM.

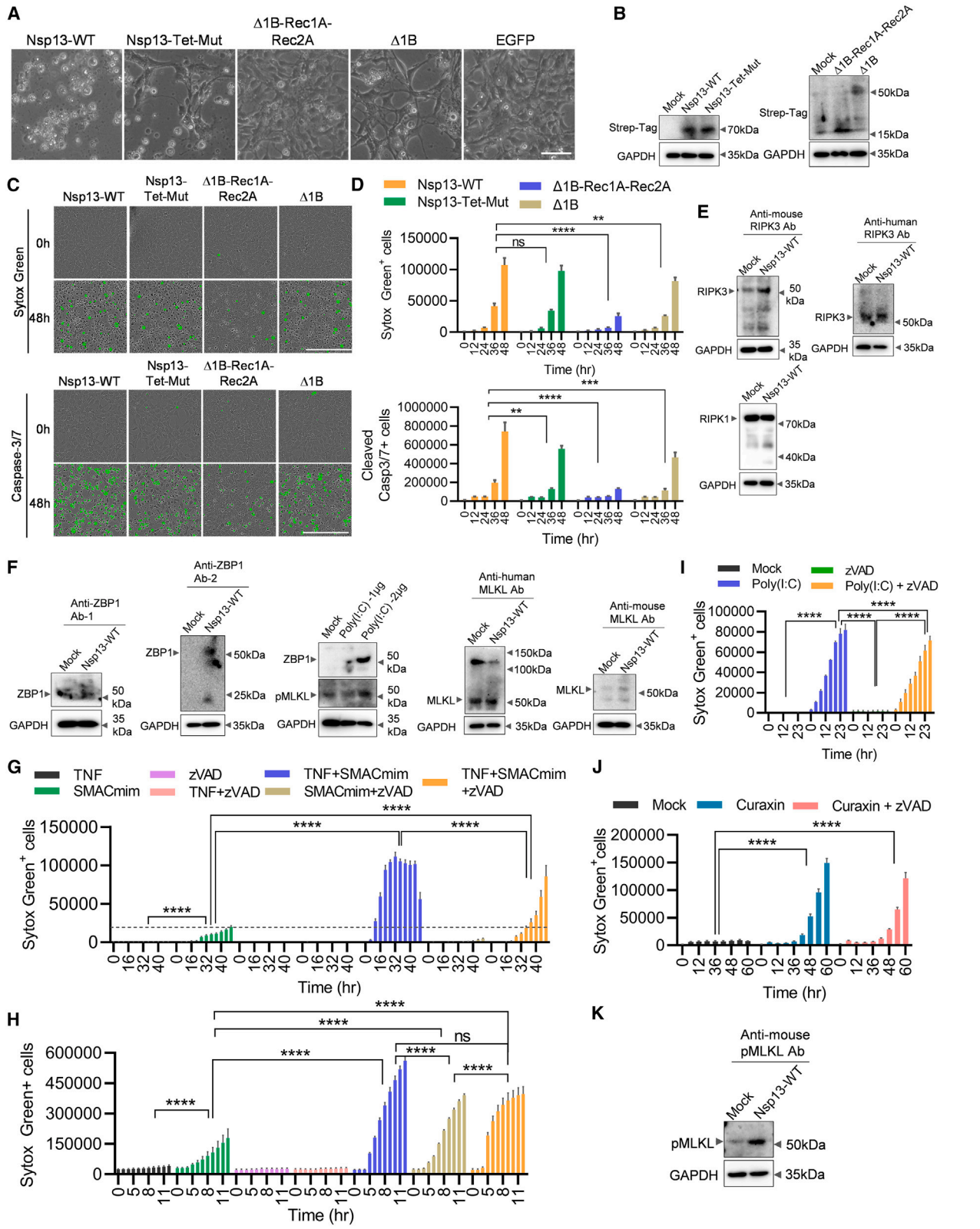


*(legend on next page)*

perturbed (Figure S1F). These observations indicate that CoV-RHIM-1 and RNA binding channel were required for Nsp13-mediated cell death. Perhaps RNA interaction with Nsp13 might facilitate RHIM-mediated cell death.

We then asked why mutating the CoV-RHIM-1 tetrad is sufficient to abolish Nsp13-mediated cell death, despite the requirement of 1B and RNA binding channel for cell death. The SARS-CoV-2 mini replication-transcription complex (RTC) consists of two Nsp13 molecules, one in apo-form (Nsp13-Apo) and the other in RNA-bound conformation (Nsp13-Rbound) (Figure S2A).[53–55] The two Nsp13 molecules are in proximity due to an interacting interface at domain 1B. Nsp13-Rbound shows a shift in its 1B domain orientation compared to Nsp13-Apo, which is critical for facilitating fully open conformation of RNA binding channel for RNA entry (Figures S2B–S2D). Using AlphaFold, we predicted the structure of Nsp13-Tet-mut and found that it attains similar conformation as Nsp13-Apo and Nsp13-Rbound (Figures S2E–S2G). However, we observed striking conformational perturbations in the vicinity of the RNA binding channel of Nsp13-Tet-mut (Figures S2B–S2G). Structural superimposition indicated that Nsp13-Tet-mut differed from Nsp13-Apo in RNA binding channel conformation (Figures S2E–S2G). Nsp13-Tet-mut attained open RNA binding channel conformation similar to Nsp13-Rbound because of the significant shift in domain 1B orientation (Figure S2G). Furthermore, the Rec2A domain of the Nsp13-tet-mut showed conformational alterations compared to Nsp13-Rbound conformation. This implicated that tetrad mutations in CoV-RHIM-1 altered the conformation of domain 1B and Rec2A in the RNA binding channel of Nsp13, which explains the Nsp13-Tet-mut mediated resistance to cell death.

## Nsp13 promotes cell death in SARS-CoV-2 infected cells and is dependent on CoV-RHIM-1 and RNA binding channel

Mutations in Nsp13 are associated with species-specific and geographical adaptation of SARS-CoV-2, and targeting Nsp13 is known to impair SARS-CoV-2 replication.[56–59] Also, substitutions in Nsp13 of CoVs severely affect replication and viral propagation.[58–62] Thus, generating Nsp13 mutants of SARS-CoV-2 is challenging. To further understand the role of Nsp13 in SARS-CoV-2-induced cell death, we ectopically expressed Nsp13-WT, Nsp13-Tet-mut, and Nsp13 lacking RNA binding channel spanning domains (Δ1B-Rec1A-Rec2A) or only 1B domain (Δ1B) in A549 cells expressing human ACE2 (A549-ACE2). We found uninfected Nsp13-WT expressing A549-ACE2 cells showed increased basal-level cell death (Figure 2F). Upon SARS-CoV-2 (Hong Kong/VM20001061/2020) infection, Nsp13-WT expressing A549-ACE2 cells showed significantly increased levels of cell death than infected mock cells (Figure 2F). However, Nsp13-Tet-mut, Δ1B-Rec1A-Rec2A, and Δ1B expressing cells showed diminished cell death than Nsp13-WT after SARS-CoV-2 infection (Figure 2F). Both uninfected and infected cells carrying Nsp13 showed increased levels of cell death compared to cells carrying Nsp13 CoV-RHIM-1 and RNA-binding channel mutants. Immunoblotting for SARS-CoV-2 nucleocapsid (N) protein in infected cells suggested productive SARS-CoV-2 infection and replication (Figure S1H). This indicates that the ectopically expressed Nsp13 was dominant over virus-encoded Nsp13, consistent with overexpression studies, and suggested that Nsp13 promotes cell death in SARS-CoV-2 infected cells. To determine whether cell death is associated with SARS-CoV-2 virus propagation or curtail infection, viral titers in infected cell supernatants were measured using a Vero-E6 cell-based plaque assay. Nsp13-WT expressing cells showed lesser viral titers in supernatant compared to mock or Nsp13-Tet-mut, Δ1B-Rec1A-Rec2A, and Δ1B expressing cells upon SARS-CoV-2 infection (Figure 2G). Cell death rate and viral titers in SARS-CoV-2 infected Nsp13-WT expressing cells indicate that Nsp13-mediated cell death restricted SARS-CoV-2 viral propagation *in vitro*.

## CoV-RHIM-1 is less critical for Nsp13-mediated cell death in bat-lung-derived Tb1 Lu cells

Viral RHIMs are known to regulate species-specific cell death programs.[24,31,34] Bats are the natural reservoir hosts for SARS-CoV-2-like viruses and likely promote viral RHIM evolution in them. Thus, we evaluated whether Nsp13 promotes or restricts RHIM-mediated cell death in a bat lung cell line (Tb1 Lu). Lentivirus virus-based SARS-CoV-2 Nsp13 expression promoted cell death in Tb1 Lu cells like in human cells (Figures 3A and 3B). Sytox green staining indicated a lower magnitude of cell death than human cells (Figures 3C and 3D). However, Caspase-3/7 dye and Sytox green staining indicated that Nsp13 expressing Tb1 Lu cells showed a high magnitude of apoptosis and detectable levels of necrotic cell death. Interestingly, mutating CoV-RHIM-1 in Nsp13 significantly decreased apoptosis

**Figure 3. Nsp13 promotes RNA-binding channel-dependent bat cell death, and CoV-RHIM-1 function is less critical**

(A) Microscopic analysis of Tb1 Lu cells infected with lentiviruses expressing SARS-CoV-2 Nsp13-WT, Nsp13-Tet-mut, Nsp13-Δ1B, Nsp13- Δ1B-Rec1A-Rec2A and EGFP followed by puromycin treatment. Scale bar, 50μm.

(B) Immunoblot analysis of lysates from Tb1 Lu cells showing expression of Nsp13-WT and its mutants after lentivirus transduction.

(C) Representative Caspase-3/7 and Sytox green staining images of Tb1 Lu cells infected with lentiviruses expressing SARS-CoV-2 Nsp13-WT, Nsp13-Tet-mut, Nsp13-Δ1B and Nsp13- Δ1B-Rec1A-Rec2A followed by puromycin treatment acquired by Incucyte imaging analysis system. Scale bar, 200μm.

(D) Real-time cell death measurement by Caspase-3/7 and Sytox green staining of Tb1 Lu cells infected as in panel-C. ****$p < 0.0001$, ***$p = 0.0003$, **$p = 0.0046$ (Sytox green staining), **$p = 0.0086$ (Caspase-3/7 staining), ns, not significant (two-way ANOVA, $n = 3$). Data shown are mean ± SEM.

(E and F) Immunoblot analysis of RIPK1, RIPK3, ZBP1 and MLKL in lysates from 'Tb1Lu cells after mock treatment, Nsp13 or Poly(I:C) transfection. The antibodies used for detecting these proteins were specific to human and mouse proteins.

(G and H) Real-time cell death measurement by Sytox green staining of Tb1 Lu (G) and HT-29 cells (H), after treatment of TNF, zVAD and SMACmimetic (SMACmim). ****$p < 0.0001$ (two-way ANOVA, $n = 3$), ns – not significant (two-way ANOVA).

(I and J) Real-time cell death measurement by Sytox green staining of Tb1 Lu cells transfected with Poly(I:C) (I) or treated with Curaxin (J) ****$p < 0.0001$ (two-way ANOVA, $n = 3$). Data shown are mean ± SEM.

(K) Immunoblot analysis of phosphorylated MLKL (pMLKL) in lysates from Tb1Lu cells after mock or Nsp13 transfection.

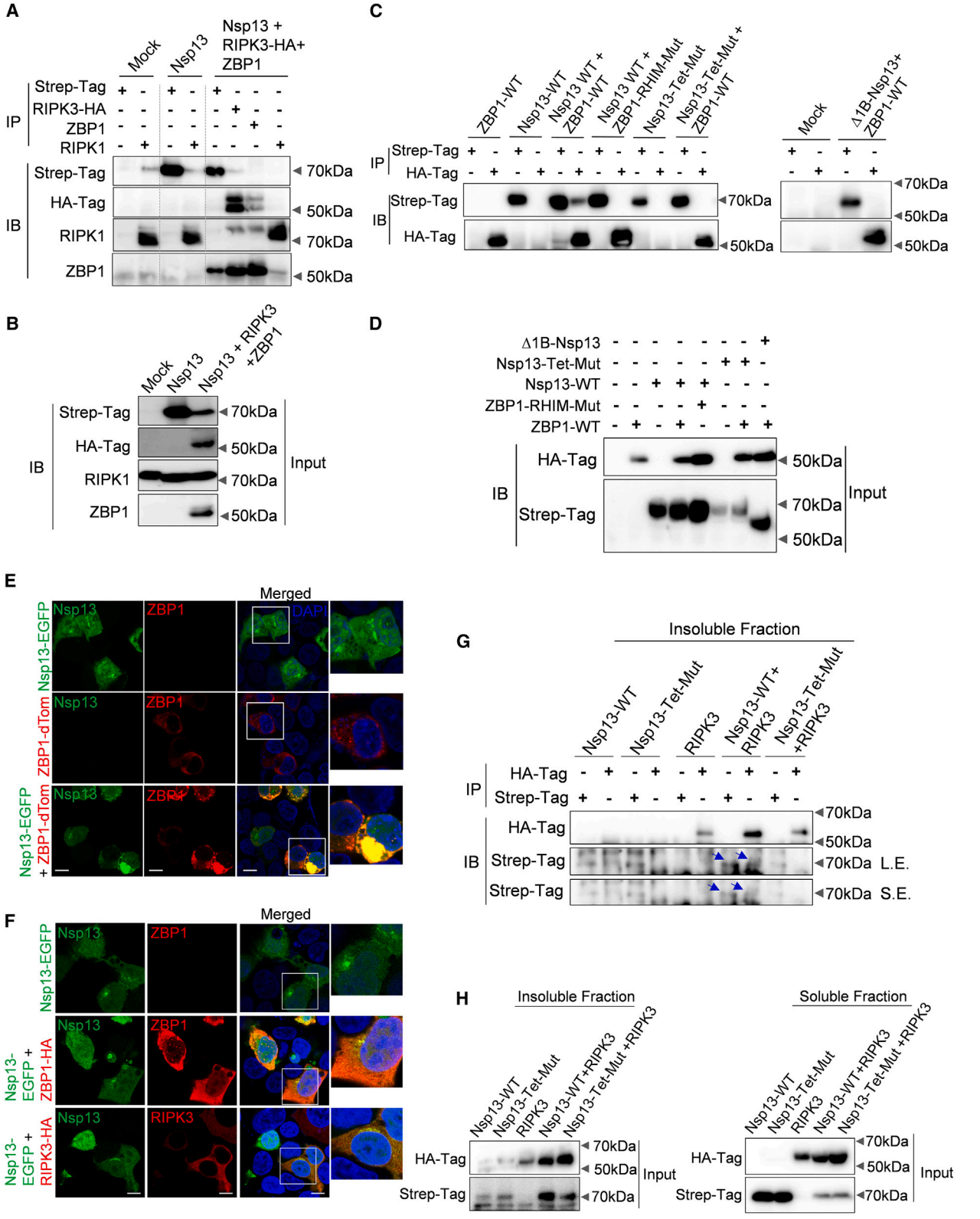


*(legend on next page)*

(Caspase-3/7) compared to necrotic cell death (Sytox green) (Figures 3C and 3D). Domain deletions affecting RNA binding channel diminished apoptosis and necrotic cell death in Nsp13 expressing Tb1 Lu cells. Also, transient expression of Nsp13 induced Tb1 Lu cell death in a dose-dependent manner and disrupting RNA binding channel reduced cell death than CoV-RHIM-1 mutant (Figures S3A–S3D). These observations indicate that Nsp13 promoted cell death, preferentially apoptosis, in bat Tb1 Lu cells which was dependent on RNA binding channel conformation. Mutating CoV-RHIM-1 in Nsp13 marginally alleviated Nsp13-mediated Tb1 Lu cell death, unlike in human cells.

The expression of RHIM-proteins and activation of RHIM-mediated apoptosis and necroptosis in bat cells is unknown. We tested the expression of RHIM-proteins in Tb1 Lu cells using multiple commercially available antibodies against RIPK1, RIPK3, and ZBP1. We found detectable protein levels of RIPK1, RIPK3, and ZBP1 in Tb1 Lu cells (Figures 3E and 3F). Transfection of double-stranded RNA ligand, Poly(I:C), upregulated ZBP1 expression in Tb1 Lu cells (Figure 3F). We also observed the MLKL expression in Tb1 Lu cells (Figure 3F). Notably, we observed lower expression levels of RHIM proteins and MLKL in Tb1 Lu cells compared to human cells. This discrepancy in detection levels might be due to the antibodies specific to detect human and mouse proteins. The detectable levels of RHIM-proteins led us to test whether Tb1 Lu cells undergo RHIM-mediated apoptosis and necroptosis. TNF, zVAD or TNF + zVAD treatment did not induce cell death, however, TNF or TNF + zVAD in combination with SMACmimetic (SMACmim) induced robust Tb1 Lu cell death (Figure 3G). However, the cell death kinetics were slower than human cells (Figures 3G and 3H). Adding GW806742X, an MLKL-specific inhibitor, diminished TNF-induced necroptosis activation in Tb1 Lu and HT-29 cells (Figures S3E and S3F). GW806742X mediated necroptosis inhibition was more robust in HT-29 cells than Tb1 Lu cells. Poly(I:C) or ZBP1 activating Curaxin (CBL0137) also induced Tb1 Lu cell death (Figures 3I and 3J). This suggests the sensitivity of Tb1 Lu cells for RHIM-protein-mediated apoptosis and necroptosis. In line with these observations, we observed detectable MLKL phosphorylation in Tb1 Lu cells with an antibody specific to mouse MLKL phosphorylated at Ser345 (Ser358 in humans, Ser363 in bat Miniopterus species), suggesting MLKL activation in those cells during necroptosis activation (Figure S3G). These observations suggest that bat-lung-derived Tb1 Lu cells undergo cell death in response to RHIM-dependent apoptosis and necroptosis triggers. Also, ectopic expression of Nsp13 in Tb1 Lu cells promoted phosphorylation of MLKL, suggesting host RHIM-protein mediated signaling activation by Nsp13 (Figure 3K). These observations suggest that Nsp13 promotes cell death in bat Tb1 Lu cells like human cells. However, unlike human cells, the Tb1 Lu cell death mainly depends on the RNA binding channel than the CoV-RHIM-1, indicating host-specific Nsp13 mediated cell death regulation. It is unknown why Tb1 Lu cells preferentially activate RHIM-dependent apoptosis, unlike human cells. Overall, the bat-lung-derived Tb1 Lu cell line operates RHIM-dependent cell death programs.

## SARS-CoV-2 Nsp13 shows RHIM-dependent association with human RHIM-proteins

RHIM-RHIM interactions promote the assembly of cell death signaling complexes like necrosome and ripoptosome to activate apoptosis and necroptosis.[13,14,63,64] To understand Nsp13 CoV-RHIM-1 role in host-RHIM-driven cell death, we ectopically expressed Nsp13 and its mutants in HT-29 cells and treated them with TNF and SMACmimetic (TNF+SMACmim) for TNF-induced apoptosis and TNF+SMACmim+zVAD for TNF-induced necroptosis (Figure S4A). As expected, these triggers induced robust cell death in HT-29 cells (Figure S4A). Expression of Nsp13-WT, Nsp13-Tet-mut, or Nsp13-Swap-mut did not diminish TNF-induced apoptosis and necroptosis in HT-29 cells, suggesting a dispensable role of Nsp13 in RIPK1-RIPK3 signaling (Figure S4A). RHIM-mediated RIPK1 and RIPK3 interactions are critical for TNF-induced apoptosis and necroptosis.[15,17,18,42,65] Viral RHIM-proteins, M45, and ICPs directly interact with RIPK3 and ZBP1 through RHIM-homotypic interactions and restrict virus-induced necroptosis.[11,20,21,24] ORF20 of VZV also interacts with ZBP1 to regulate virus-induced apoptosis.[33] HSV-1 viral RHIM-protein, ICP6, shows species-specific necroptosis regulation by promoting viral-RHIM mediated necroptosis in mouse cells but restricting necroptosis activation in human cells.[24,31,34] We sought to determine the ability of SARS-CoV-2 Nsp13 to interact with human RIPK1, RIPK3, and ZBP1 by co-expressing these proteins in HEK-293T cells, followed by immunoprecipitation. HEK-293T cells express RIPK1 endogenously but do not express RIPK3 and ZBP1 proteins. When Nsp13, RIPK3, and ZBP1 were co-expressed in HEK-293T cells, immunoprecipitation with anti-HA-tag (RIPK3-HA) and anti-ZBP1 antibodies showed RIPK3-RIPK1-ZBP1 complex formation without Nsp13 (Figures 4A and 4B). Nsp13 did not show detectable interaction with RIPK1 and RIPK3, corroborating the dispensable role of Nsp13 in TNF-induced apoptosis and necroptosis (Figures 4A and 4B). However, Nsp13 immunoprecipitation showed its interaction with ZBP1. This suggests that Nsp13 can interact with ZBP1 but may not

**Figure 4. SARS-CoV-2 Nsp13 shows RHIM-dependent interaction with host ZBP1 and RIPK3 proteins**

(A and B) Immunoblot analysis of anti-Strep-Tag (Nsp13), anti-RIPK1, anti-HA-tag (RIPK3), and anti-ZBP1 immunoprecipitates (A) and whole cell lysates (inputs) (B) from HEK-293T cell lysates expressing Nsp13 alone or co-expressing Nsp13, RIPK3 and ZBP1.

(C and D) Immunoblot analysis of anti-Strep-Tag (Nsp13) and anti-HA-tag (ZBP1) immunoprecipitates (C) and inputs (D) from HEK-293T cell lysates expressing Nsp13 WT, Nsp13-Tet-Mut, Δ1B, ZBP1-WT and ZBP1-RHIM-Mut alone or in indicated combinations of Nsp13 and ZBP1 constructs.

(E) Confocal microscopy imaging of HEK-293T cells expressing Nsp13-EGFP or ZBP1-dTomoto alone or co-expressing both the constructs. Scale bar, 10μm.

(F) Confocal microscopy imaging of HEK-293Tcells expressing Nsp13-EGFP and in combination with ZBP1-HA or RIPK3-HA. Scale bar, 10μm.

(G) Immunoblot analysis of anti-Strep-Tag (Nsp13) and anti-HA-tag (RIPK3) immunoprecipitates from insoluble fractions of HEK-293T cell lysates expressing Nsp13-WT, Nsp13-Tet-Mut and RIPK3 individually or in indicated combinations of Nsp13 and RIPK3 constructs. L.E. – long exposure; S.E. – short exposure.

(H) Inputs for insoluble and soluble fractions of cell lysates for Panel-G.

interfere with host RHIM-protein interactions. To understand whether these interactions are RHIM-dependent, we sought to test the interaction of RHIM and 1B domain deletion mutants of Nsp13 with the ZBP1 through immunoprecipitation. Nsp13-WT interacted with the ZBP1-WT, but Nsp13-Tet-mut, and the Nsp13 lacking 1B did not interact with the ZBP1-WT (Figures 4C and 4D). Also, mutating the RHIM domain (RHIM-1) of the ZBP1 disrupted its interaction with the Nsp13-WT (Figures 4C and 4D). These observations further indicate that the association of Nsp13 with the ZBP1 is RHIM-dependent.

To further establish SARS-CoV-2 Nsp13 association with host-RHIM proteins, we tagged Nsp13 with EGFP (Nsp13-EGFP) for capturing Nsp13 association with RHIM proteins in imaging studies (Figures S4B–S4D). Tagging EGFP did not alter Nsp13-mediated cell death and protein expression, indicating the retention of Nsp13 native conformation upon EGFP fusion (Figures S4C and S4D). Nsp13-EGFP and ZBP1-dTomato were colocalized upon co-expression, and the colocalized regions appeared as complexes (Figure 4E). We further co-expressed Nsp13-EGFP with ZBP1 tagged with HA-Tag (ZBP1-HA) and found that Nsp13 and ZBP1 colocalize in HEK-293T cells (Figure 4F). Also, Nsp13 appeared to be colocalized with RIPK3 but not RIPK1 (Figures 4F and S4E). Real-time analysis of Nsp13-EGFP and ZBP1-dTomato expression in live cells showed colocalization of Nsp13 with the ZBP1 upon expression and led to cell death phenotype (Figure S4F). The co-expression of Nsp13 with the RHIM-mutant of ZBP1 reduced Nsp13-ZBP1 colocalization, suggesting RHIM-dependent association (Figures S4G and S4H). These observations further indicate the association of Nsp13 with the ZBP1 and RIPK3 and higher-order complex formation. Although we did not observe Nsp13 and RIPK3 interaction in immunoprecipitation experiments, imaging studies show that Nsp13 colocalized with RIPK3 (Figure 4F). To validate this further, we separated soluble and insoluble fractions from the whole cell lysates co-expressing Nsp13-WT or Nsp13-Tet-mut with RIPK3 and subjected to immunoprecipitation with Strep-tag and HA-tag antibodies. We observed detectable interaction of RIPK3 with Nsp13 in the insoluble fraction but not in the soluble fraction (Figures 4G and S4I). Moreover, Nsp13 and RIPK3 were present in soluble fractions when expressed individually, and significant protein fractions of Nsp13 and RIPK3 appeared in insoluble fractions when co-expressed (Figure 4H). These observations further indicate the association of Nsp13 with RIPK3 and ZBP1.

### SARS-CoV-2 Nsp13 promotes the formation of large insoluble complexes of RHIM proteins

Recent studies demonstrated the formation of RHIM-driven insoluble amyloid-like complexes by RIPK1, RIPK3, and ZBP1 upon interaction with viral-RHIM proteins.[14,32,63,66] To monitor whether SARS-CoV-2 Nsp13 can assemble large complexes, we expressed Nsp13 and its mutants alone or in combination with RIPK3 and ZBP1 in HEK-293T cells. To preserve oligomeric complexes, cell lysates were crosslinked using a DSP cross-linker, which has a built-in disulfide in its spacer region that allows decoupling of crosslinked oligomers through treatment with disulfide reducing agents such as beta-mercaptoethanol (BME). Nsp13-WT expression formed NP-40 soluble higher-order complexes with undetectable oligomers in the insoluble fraction (Figure S5A). We observed an increased complex formation by Nsp13-Tet-mut and Nsp13-Swap-mut than Nsp13-WT in NP40-soluble fractions (Figure S5A). Thus, SARS-CoV-2 Nsp13 appeared to oligomerize into large complexes upon overexpression, and mutating or swapping core tetrad of CoV-RHIM-1 further enhanced homo-oligomer formation. This indicated the predominant monomeric nature of the Nsp13-WT protein, which might oligomerize when 1B domain conformation is perturbed. Since Nsp13 interacted with ZBP1 in HEK-293T cells, we further monitored whether Nsp13 affects ZBP1 oligomerization. We observed detectable but low levels of higher-order oligomers of ZBP1 in NP40-insoluble fraction upon transfection (Figure S5A). Co-expression of ZBP1 with Nsp13-WT showed significantly increased levels of ZBP1 oligomers in NP-40 insoluble fraction (Figure S5A). However, Nsp13-Tet-mut and ZBP1 co-expression showed a lesser magnitude of ZBP1 oligomer formation (Figure S5A). In contrast to the predominant monomeric form of Nsp13-WT, its co-expression with ZBP1 showed detectable levels of Nsp13-WT complexes in NP40-insoluble fraction and increased levels of oligomers in NP40-soluble fraction (Figure S5A). These crosslinking experiments suggested that Nsp13 promotes CoV-RHIM-dependent ZBP1 complex formation. As Nsp13-Tet-mut already forms non-native oligomers, its expression with ZBP1 did not facilitate ZBP1 complex formation (Figure S5A).

We further co-expressed Nsp13-WT with RIPK3 and ZBP1 and monitored higher-order complex formation. The co-expression of ZBP1 and RIPK3 led to the formation of NP-40 soluble and insoluble RIPK3 oligomers (Figure 5A). These oligomers were dissolved into monomers upon BME treatment (Figure 5A). However, ZBP1 did not show detectable oligomerization in both fractions (Figure 5A). Similarly, the co-expression of Nsp13-WT with RIPK3 triggered RIPK3 complex formation in NP40-insoluble and soluble fractions. Higher order complexes of the RIPK3 were observed even when RIPK3 was expressed with Nsp13-WT and ZBP1. The magnitude of oligomer formation was lesser than that was seen in Nsp13-WT and RIPK3 co-expressed cell lysates (Figure 5A). ZBP1 formed NP40-insoluble complexes when co-expressed with Nsp13-WT or Nsp13-WT and RIPK3 (Figure 5A). Even though BME treatment decoupled the complexes of RIPK3 and ZBP1, a fraction of complexes was not completely dissolved after BME treatment, suggesting the formation of insoluble higher-order complexes with hydrophobic interfaces as reported previously for host RHIM-proteins (Figure 5A).[32,63] These observations suggest that Nsp13 forms soluble higher-order complexes when co-expressed with RIPK3 or ZBP1. Nsp13 co-expression promotes insoluble complexes of RIPK3 and ZBP1. Thus, Nsp13 may preferably form soluble oligomers that further nucleate RIPK3 and ZBP1 insoluble necrosome-like assemblies.

To further understand the association of Nsp13 with ZBP1 and RIPK3, we visualized Nsp13, ZBP1, and RIPK3 in HEK-293T cells using DNA-PAINT imaging that enables nanometer-scale resolution for monitoring complex formation. DNA-PAINT imaging suggested spatial localization of Nsp13 with ZBP1 and RIPK3

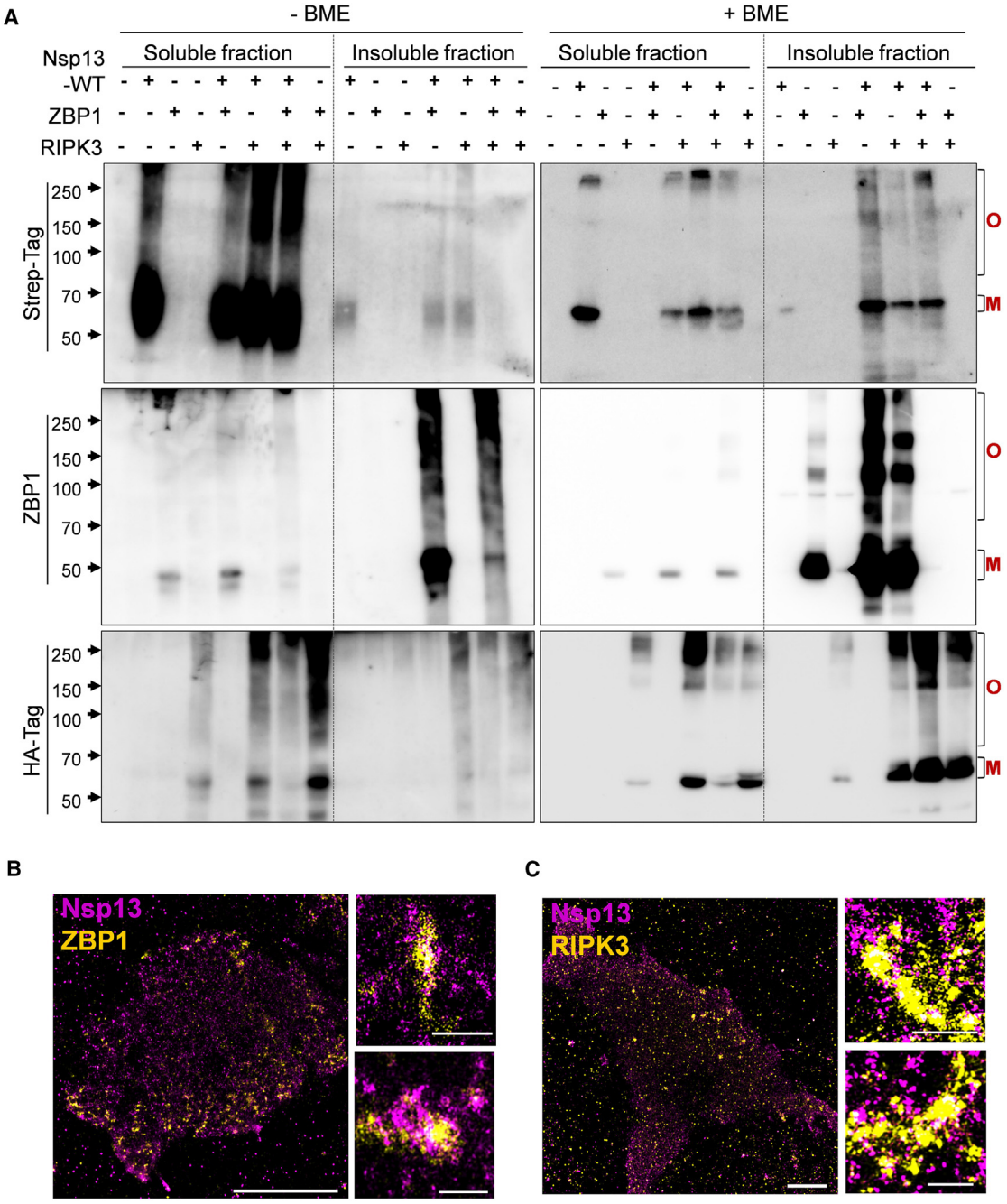


**Figure 5. SARS-CoV-2 Nsp13 triggers host-RHIM protein oligomerization and large complex formation**

(A) Immunoblot analysis of crosslinked lysates of HEK-293T cells expressing Nsp13-WT, RIPK3 and ZBP1 individually or co-expressing Nsp13-WT+ZBP1, Nsp13-WT+RIPK3, Nsp13-WT+ZBP1+RIPK3 or ZBP1+RIPK3, in non-reduced (without BME) and reduced (with BME) conditions. O- oligomer complexes; M-Monomer.

(B and C) Visualization of SARS-CoV-2 Nsp13 and ZBP1 (B) or RIPK3 (C) in HEK-293T cells using DNA-PAINT imaging. Scale bars, 5 μm (complete cell image); 200nm (magnified images).

(Figures 5B, 5C, S5B, and S5C). A recent study showed the formation of round and rod-shaped RHIM-protein amyloid complexes using super-resolution microscopy.[66] ZBP1 appeared as rod-shaped complexes in Nsp13-ZBP1 complexes compared to Nsp13 (Figures 5B and S5B). RIPK3 appeared as round and rod-shaped structures in Nsp13-RIPK3 complexes (Figures 5C and S5C). The DNA-PAINT imaging indicated the formation of round and rod-shaped complexes by ZBP1 and RIPK3. Nsp13 is in proximity with ZBP1 and RIPK3 in complexes, although Nsp13 appeared to form smaller and more distinct

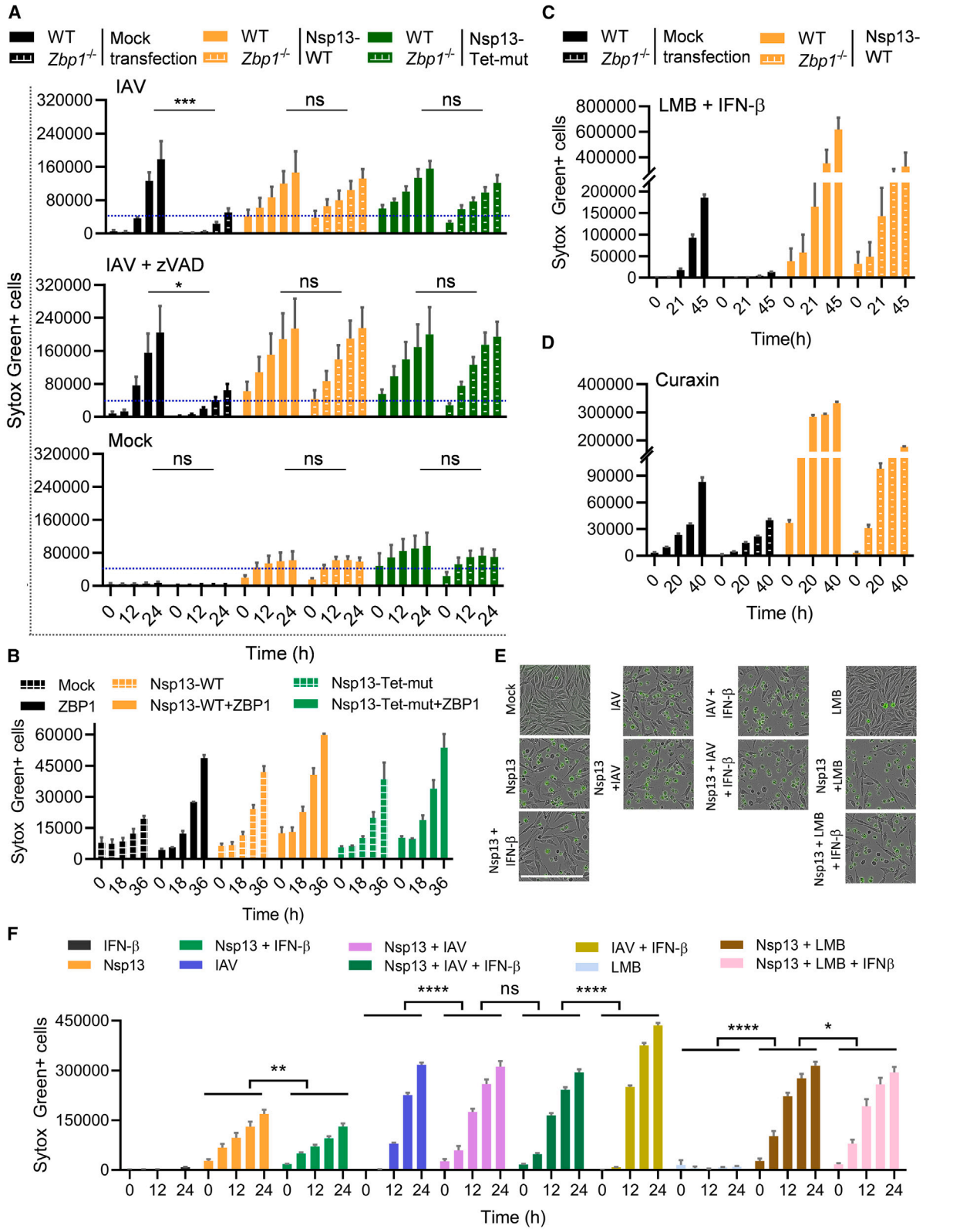


*(legend on next page)*

structures than ZBP1 and RIPK3. Together, these observations indicate that Nsp13 employs viral RHIMs to promote the higher-order complex formation.

## SARS-CoV-2 Nsp13 promotes ZBP1-RIPK3 signaling and cell death

Higher-order complex formation by ZBP1 and Nsp13 after co-expression led us to examine the role of Nsp13 in ZBP1-RIPK3 signaling-specific cell death activation. ZBP1 activation triggers IAV-induced necroptosis, apoptosis and pyroptosis cell death programs. Most transformed human cell lines do not express RIPK3 and ZBP1. L929 cells (mouse fibroblast cell line) retain ZBP1 expression and show ZBP1-dependent cell death after IAV infection. Thus, we generated *Zbp1*$^{-/-}$ L929 cells to study the role of Nsp13 in ZBP1-dependent cell death pathways. We transiently expressed Nsp13 in WT and *Zbp1*$^{-/-}$ L929 cells and infected these cells with IAV to study the role of Nsp13 in IAV-induced necroptosis (Figure 6A). Without Nsp13 expression, *Zbp1*$^{-/-}$ cells showed significantly less cell death than WT cells after IAV infection or IAV combined with zVAD treatment (IAV + zVAD, for activating necroptosis). Nsp13-WT expression in WT cells did not inhibit IAV or IAV+zVAD-induced cell death and promoted faster kinetics of cell death activation (Figure 6A). Interestingly, NSP13-WT expressing *Zbp1*$^{-/-}$ cells showed a higher magnitude of cell death, which is comparable to WT-cells, suggesting the role of Nsp13 in promoting IAV-induced cell death in the absence of ZBP1 (Figure 6A). Immunoblotting analysis showed that Nsp13-WT expression in *Zbp1*$^{-/-}$ cells led to increased pMLKL levels than *Zbp1*$^{-/-}$ cells without Nsp13 expression (Figure S5D). This indicated IAV+zVAD-mediated necroptosis activation by Nsp13 despite lacking ZBP1 expression. However, Nsp13-Tet-mut expression in *Zbp1*$^{-/-}$ cells did not reduce IAV or IAV+zVAD-induced cell death, suggesting that mutating core tetrad of CoV-RHIM-1 does not appear to abolish Nsp13-induced cell death in IAV-infected *Zbp1*$^{-/-}$ cells (Figure 6A). Nsp13-WT and Nsp13-Tet-mut expressing WT and *Zbp1*$^{-/-}$ cells showed a very low magnitude of cell death without infection than IAV and IAV+zVAD treatment (Figure 6A). To further understand whether Nsp13 promotes ZBP1-dependent cell death in human cells, we infected HT-29 cells with IAV+zVAD. HT-29 cells express RIPK3 but show undetectable ZBP1 expression. Expression of human ZBP1 in HT-29 cells led to increased necroptosis activation after IAV+zVAD treatment (Figure 6B). Nsp13-WT co-expression with ZBP1 enhanced IAV+zVAD-induced necroptosis in HT-29 cells (Figure 6B). Thus, it appeared that Nsp13 promoted ZBP1-induced cell death during IAV infection. Intriguingly, Nsp13 promoted IAV-induced cell death in the absence of ZBP1 expression.

Leptomycin-B (LMB), in combination with IFNs or curaxin (CBL0137) treatment, is known to trigger ZBP1 activation and cell death.[41,67] We examined LMB+IFN-β and curaxin-mediated cell death in WT and *Zbp1*$^{-/-}$ L929 cells to further probe the role of SARS-CoV-2 Nsp13 in ZBP1 function (Figures 6C and 6D). As expected, LMB+IFN-β treatment triggered cell death, and lack of ZBP1 significantly abolished this cell death (Figure 6C). However, upon Nsp13-WT expression in *Zbp1*$^{-/-}$ cells, increased cell death was observed after LMB+IFN-β treatment compared to those without Nsp13-WT expression (Figure 6C). Curaxin treatment in WT and *Zbp1*$^{-/-}$ cells showed ZBP1-dependent cell death activation, and Nsp13-WT expression led to increased cell death in *Zbp1*$^{-/-}$ cells similar to that of LMB+IFN-β treatment (Figure 6D). Nsp13-WT overexpression further enhanced cell death in WT cells after LMB+IFN-β or curaxin treatment (Figures 6C and 6D). These results further suggest that SARS-CoV-2 Nsp13 promotes ZBP1-mediated cell death, and in the absence of ZBP1 expression, Nsp13 triggers cell death in response to ZBP1 activating ligands. Why might Nsp13 have evolved to regulate ZBP1-RIPK3 signaling and induce host cell death? Type I interferons (IFN) promote ZBP1 and RIPK3 signaling and activation of cell death in viral infections.[9,22,41,42,68] Delayed type I IFN production and restricted IFN signaling due to Nsp13 and other proteins of SARS-CoV-2 facilitate host modulation and efficient virus propagation.[1,8] We anticipate that the dampened type I IFN signaling might restrict early activation of ZBP1-RIPK3 signaling and cell death, which preferentially destroy viral replication platforms. Perhaps Nsp13 has evolved to trigger cell death due to insufficient ZBP1-RIPK3 signaling activation at the late stages of the infection to facilitate viral spread, tissue damage, and inflammation. Indeed, recent studies demonstrate IFN and inflammatory cytokine-driven cell death, tissue damage, and disease pathogenesis during SARS-CoV-2 infection at later stages.[1,12,69–71]

## Intracellular RNA ligands and type I IFNs regulate SARS-CoV-2 Nsp13-mediated cell death

Type I IFNs upregulate ZBP1 and MLKL expression and promote necroptosis and other programmed cell death activation in viral infections.[9,41,42,68] SARS-CoV-2 Nsp13 is associated with innate immune evasion and restricts type I IFN signaling activation.[8] We hypothesize that type I IFN treatment may regulate Nsp13-mediated cell death. Ectopic expression of Nsp13 in L929 cells promoted spontaneous cell death at the basal level, and IFN- β treatment partly reduced this Nsp13-induced cell death, suggesting IFN receptor-mediated cell death regulation (Figures S5E and S5F). Nsp13-mediated cell death requires CoV-RHIM in 1B domain and RNA binding channel (spanning 1B,

**Figure 6. SARS-CoV-2 Nsp13 promotes ZBP1-RIPK3 signaling-dependent cell death and is regulated by intracellular RNA ligands**

(A) Real-time cell death measurement by Sytox green staining of WT and *Zbp1*$^{-/-}$ L929 cells ectopically expressing Nsp13-WT and Nsp13-Tet-mut after IAV, IAV+zVAD and mock infection. ***$p$ = 0.0005, *$p$ = 0.0307, ns, not significant (two-way ANOVA).

(B) Real-time cell death measurement by Sytox green staining of ZBP1 expressing HT-29 cells after Nsp13 transfection and IAV+zVAD infection.

(C and D) Cell death measurement by Sytox green staining of WT and *Zbp1*$^{-/-}$ L929 cells expressing Nsp13-WT after LMB+IFN-β (C) and Curaxin (D) treatment. Data shown are mean ± SEM.

(E) Microscopic images of cell death in L929 treated as indicated and acquired by Incucyte imaging analysis for the cells. Scale bar, 200μm.

(F) Real-time analysis of cell death of mock or Nsp13 transfected L929 cells treated/infected with IFN-β alone, IAV alone, IAV + IFN-β, LMB alone or LMB + IFN-β. ****$p$ < 0.0001, **$p$ = 0.0022, *$p$ = 0.0310, ns, not significant (two-way ANOVA, $n$ = 3). Data shown are mean ± SEM.

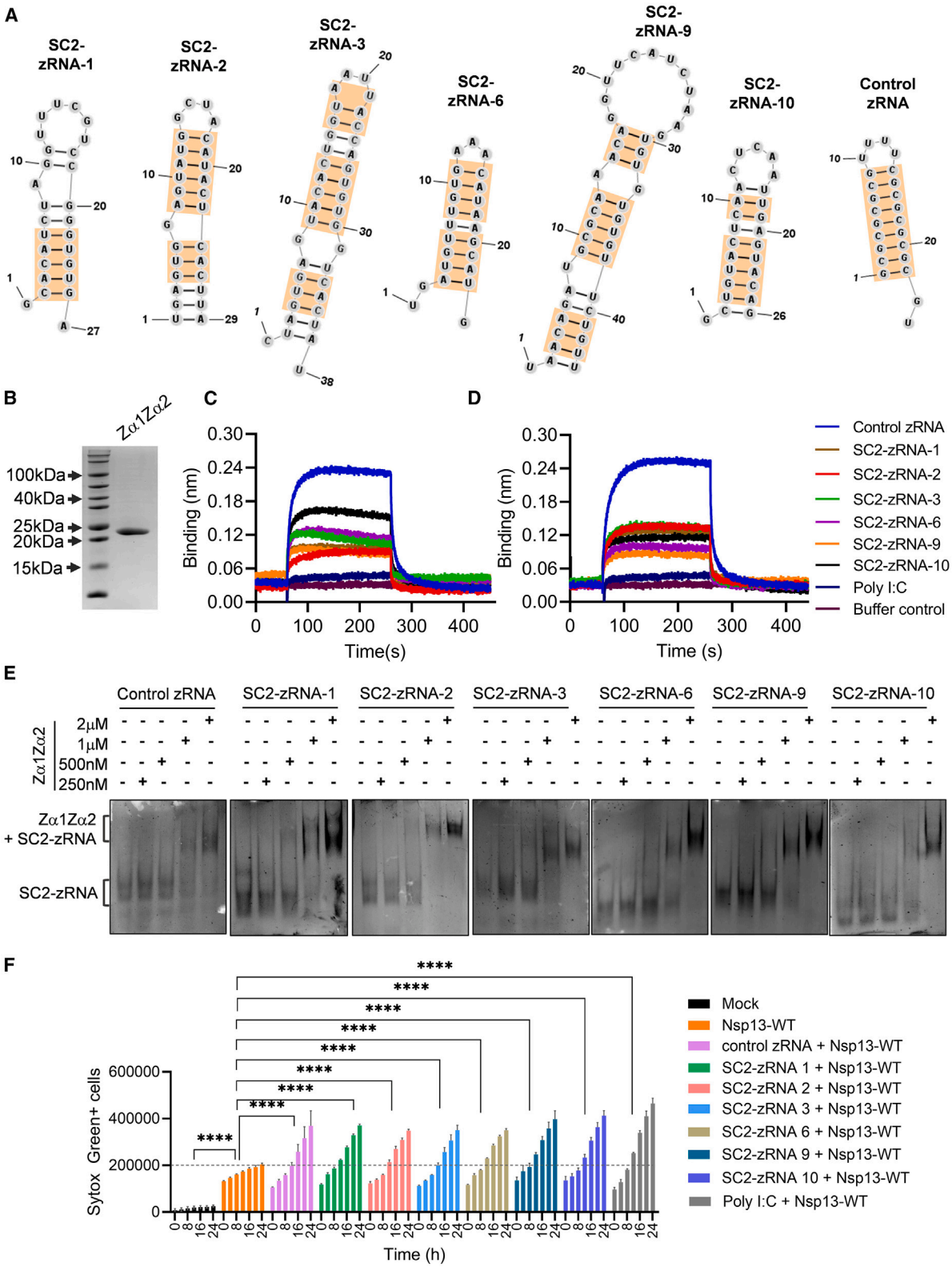


*(legend on next page)*

Rec1A, and Rec2A domains), suggesting RNA binding as a critical step for cell death activation by Nsp13. Intracellular delivery of Poly(I:C) (transfection) increased Nsp13-mediated cell death, but the addition of Poly(I:C) to the cell surface did not alter Nsp13-mediated cell death (Figures S5G and S5H). As expected, IAV infection in Nsp13-expressing cells promoted increased cell death (Figures 6E and 6F). However, unlike IFN-β-dependent inhibition of Nsp13-mediated cell death, IFN-β treatment after IAV infection in Nsp13-expressing cells did not reduce cell death (Figures 6E and 6F). Without Nsp13 expression, IAV and IFN-β treatment showed a further increase in cell death levels. Furthermore, LMB treatment in Nsp13-expressing cells showed a higher magnitude of cell death activation than in Nsp13-expressing untreated cells (Figures 6E and 6F). LMB+IFN-β treatment did not alter Nsp13-mediated cell death. These observations suggested that IFN-β did not inhibit Nsp13-mediated cell death during IAV infection or LMB treatment, which generates intracellular RNA ligands. Thus, these results further indicate the requirement of RNA ligand binding in Nsp13-mediated cell death and the regulation of this cell death by type I IFNs.

### The SARS-CoV-2 genome shows Z-RNA signatures, binds to Zα domains of ZBP1, and promotes Nsp13-mediated cell death

The role of Nsp13 in promoting cell death, interacting with host RHIM-proteins, and its ability to promote ZBP1 signaling suggest the association of Nsp13 with Z-RNAs. We hypothesize that the SARS-CoV-2 RNA genome consists of base repeats favoring Z-RNA conformation and are generated during its replication process. The repeats of purine and pyrimidine (Pu:Py), predominantly (CG)n, (UG)n/(TG)n, (CA)n, favor Z-RNA/Z-DNA conformation.[30,72–74] Also, short interspersed nuclear elements (SINEs) with inverted repeat sequences increase the propensity of RNA to attain Z-conformation.[41,67,75,76] We have devised a comprehensive analysis, incorporating alternate Pu:Py, inverted tandem repeats, SINEs, and the sequences favoring double-strand RNA formation, for identifying Z-RNA segments in the SARS-CoV-2 genome. We found that Z-RNA-like sequences were distributed across the SARS-CoV-2 genome, but most of these sequences span ORF1a and ORF1b of the genome (Figure S6A). We further predicted the RNA secondary structures of these potential Z-RNA hotspots using RNAstructure prediction server (Figures 7A and S6B). Among these Z-RNA forming double-stranded RNA (dsRNA) structures, we selected dsRNAs in which alternate Pu:Py repeats stabilized the secondary structure. We identified several SARS-CoV-2 genome hotspots with Z-RNA-favoring sequences using this approach. Recent studies experimentally determined the secondary structure of the SARS-CoV-2 genome in infected cells.[77–79] The predicted secondary structures of Z-RNA sequences were mapped on the experimentally solved secondary structures of the SARS-CoV-2 genome to check if they retained the same structures as the prediction. Using this secondary structure comparison, the candidate Z-RNAs, which retain the dsRNA conformation in experimentally solved SARS-CoV-2 genome structure, were identified (Figures 7A and S6B). The identified Z-RNAs forming secondary structures span the SARS-CoV-2 Nsp1, Nsp2, Nsp3, Nsp4, Nsp6, Nsp13, and Nsp16 coding regions of ORF1ab (Figure S6B). By examining the experimentally determined SARS-CoV-2 genome secondary structure, we further identified additional genome sequences with Z-RNA forming propensity in N-protein coding regions. Together, our rational sequence and structure-based mining of the SARS-CoV-2 genome identified the sequences with high Z-RNA forming propensity.

To further validate the ability of SARS-CoV-2 Z-RNAs (SC2-zRNA) for binding Z-RNA sensing proteins, we purified Zα domains of human ZBP1 (Zα1-Zα2) to probe its binding to SC2-zRNAs using real-time biolayer interferometry and electrophoretic mobility shift assays (EMSA) (Figure 7B). SC2-zRNAs segments were generated by *in vitro* transcription for binding studies with Zα1-Zα2. We mutated one of the surface-accessible serine residues in Zα2 domain to cysteine (S106C) for labeling purified Zα1-Zα2 protein. Using biolayer interferometry (BLI-Octet) we examined the real-time binding of *in vitro* transcribed SARS-CoV-2 RNA segments with high Z-RNA propensity (SC2-zRNA-1,2,3,6,9 and 10) to purified Zα1-Zα2 (Figures 7C and 7D). In this analysis, we included poly(I:C) and a Pu:Py repeat RNA that attain Z-RNA conformation (control zRNA) when incorporated with modified guanine bases.[67,80] The control zRNA bound to Zα1-Zα2 protein with high association rates (despite lacking modified guanines) and poly(I:C), and buffer controls bound with very low association rates (Figures 7C and 7D). Perhaps Zα1-Zα2 binding might have driven the attainment of stable Z-conformation in control zRNA despite lacking modified bases. The SC2-zRNA bound to Zα1-Zα2 protein with higher association rates than poly(I:C) and buffer control but less than the control zRNAs (Figures 7C and 7D). Notably, the dissociation of control zRNA and SC2-zRNAs from Zα1-Zα2 protein was similar. These observations indicate that the selected SARS-CoV-2 RNA genome segments attain z-RNA conformation and bind to Zα1-Zα2 protein without the requirement of incorporating modified bases in SC2-zRNAs. Furthermore, we performed EMSAs to monitor SC2-zRNAs interaction with Zα1-Zα2 protein. Although we attempted to label Zα1-Zα2 protein by cysteine maleimide labeling for fluorescence imaging of EMSA gels, the labeled

**Figure 7. SARS-CoV-2 encode Z-RNA forming genomic segments that enhance Nsp13-mediated cell death**

(A) Specific SARS-CoV-2 genome segments with high Z-RNA forming dsRNA conformations. The orange box outlines represent alternate purine-pyrimidine repeats with Z-RNA forming and Zα-domain binding potential.

(B) SDS-PAGE gel picture representing purified human ZBP1-Zα1α2 domains.

(C and D) Octet binding of SARS-CoV-2 Z-RNAs (SC2-zRNA), control Z-RNA (alternate purine-pyrimidine repeats favoring Z-RNA conformation) and poly(I:C) at 100nM (D) and 200nM (E) concentration to human ZBP1-Zα1α2 domains.

(E) Electrophoretic mobility shift assay of control Z-RNA and SARS-CoV-2 Z-RNAs with human ZBP1-Zα1α2 domains to monitor their interaction.

(F) Real-time cell death measurement by Sytox green staining of Nsp13 expressing L929 cells after transient transfection with control zRNA, SARS-CoV-2 Z-RNAs (SC2-zRNA) or Poly(I:C). ****$p < 0.0001$ (two-way ANOVA, $n = 3$). Data shown are mean ± SEM.

protein was degraded rapidly. We further proceeded to use unlabeled protein for EMSA studies. We observed that control zRNA and SC2-zRNAs showed detectable shifts in zRNA sizes, indicating the binding of SC2-zRNAs with Zα1-Zα2 protein (Figure 7E). These band shifts were observed at higher Zα1-Zα2 protein concentrations, perhaps because of the faster dissociation rates observed in real-time BEI-Octet analysis (Figure 7E). The EMSA experiments further establish that SARS-CoV-2 RNA genome segments attain Z-RNA conformation and bind to Z-RNA sensing Zα domains. Since intracellular RNA ligands regulate Nsp13-mediated cell death, we tested whether SC2-zRNAs promote Nsp13-mediated cell death. Nsp13-expressing L929 cells showed enhanced cell death levels after intracellular delivery of SC2-zRNAs or Poly(I:C) compared to mock-transfected Nsp13-expressing cells (Figure 7F). SC2-zRNAs showed a low magnitude of cell death in the absence of Nsp13 expression (Figure S6C). These observations suggest that SC2-zRNAs regulate SARS-CoV-2 Nsp13-mediated cell death.

Computational docking studies showed that all the SARS-CoV-2 Z-RNAs were docked into the RNA binding channel of the Nsp13 (Figure S7A). Most of these Z-RNAs showed lesser binding energies than the random RNA sequences tested (Figure S7B). To examine how SARS-CoV-2 Z-RNA binding to Nsp13 regulates Nsp13 association with the host RHIMs, we performed protein-protein docking with Z-RNA bound Nsp13 and RHIM of the RIPK3 as the ZBP1-RHIM structure was not available. We docked Nsp13 structure with RIPK3-RHIM structure (PDB ID: 6JPD), which is in oligomeric firbril complex. The docked structures showed that the RIPK3 RHIM is in proximity to the 1B domain of Nsp13 (that harbor CoV-RHIM) (Figures S7C–S7E). We observed that Nsp13 bound to SARS-CoV-2 zRNA (SC2-zRNA-2 and SC2-zRNA-6) structures showed increased accessibility of CoV-RHIM and its proximity with the RHIM of the RIPK3 (Figures S7D and S7E). RNA unbound structure of Nsp13 showed less accessibility of CoV-RHIM to engage RHIM of RIPK3 and distorted RHIM-RHIM orientation (Figure S7C). However, in both RNA-bound and unbound structures, we did not observe significant alterations in the conformation of CoV-RHIM of Nsp13. Based on these observations, we speculate that Z-RNA binding to Nsp13 promotes CoV-RHIM accessibility and its interaction with the host RHIMs for regulating cell death.

## DISCUSSION

Our findings in this report indicate that Nsp13 and Nsp14 of CoVs harbor putative RHIMs. Viral RHIMs reported to date were found in DNA viruses, and our study identified and characterized viral RHIMs of RNA viruses. SARS-CoV-2 Nsp13 is a viral RHIM protein promoting human cell death programs. Our analysis further reveals bats as an essential source in the evolution of viral RHIMs in pathogenic RNA viruses. It was intriguing to find that, unlike the viral RHIMs reported to date, SARS-CoV-2 Nsp13 did not inhibit cell death and instead promoted it in specific conditions. A recent study indicated an RHIM-like sequence signature in SARS-CoV-2 Nsp13 based on protein sequence analysis.[81] Our protein sequence and structure-based analysis of the CoV family revealed CoV-RHIMs in Nsp13 and Nsp14 proteins and their association with bat-originated CoVs. Moreover, the CoV-RHIMs in Nsp13 and Nsp14 showed a distinct pattern of evolution. CoV-RHIM-1 in Nsp13 showed a conserved RHIM sequence pattern in pathogenic human-CoVs and bat-associated beta-CoVs, whereas CoV-RHIMs of Nsp14 are conserved in less pathogenic human-CoVs. Our analysis might facilitate RHIM sequence-based annotation of new bat-CoVs or CoVs that have not infected humans for their possible pathogenic potential. How did Nsp13 and Nsp14 acquire RHIMs mimicking host RHIM-proteins? Bats express RIPK3 and ZBP1 proteins. The conserved CoV-RHIMs in bat-originated CoVs raise the possibility that bat RIPK3 and ZBP1 might have driven the evolution of RHIMs in CoVs to modulate their function. Also, how bats show only mild clinical symptoms despite hosting SARS-CoV-2-like viruses is unknown. RHIM-mediated cell death, the evolution of viral RHIMs, and RHIM-driven virus-host interactions might provide new clues for understanding viral tolerance in bats. Our observations indicate that RNA viral RHIM proteins, like Nsp13, show distinct cell death regulatory mechanisms in bat-derived Tb1 Lu and human cells. Nsp13 preferentially promotes apoptosis of bat cells, which is less dependent on CoV-RHIM-1 but requires RNA-binding channel function. However, Nsp13 triggers apoptotic and necrotic-like cell death in human cells that depend on CoV-RHIM-1 and RNA binding channel. Thus, bats might have evolved to employ additional mechanisms for modulating viral RHIM-mediated cell death to alleviate viral RHIM-mediated detrimental effects. Our results showing the detectable expression of RHIM proteins in bat-derived Tb1 Lu cells and their sensitivity to RHIM-dependent cell death triggers suggest that Tb1 Lu cells operate RHIM-mediated signaling albeit less robustly than human cells.

Nsp13 is a helicase protein and a component of the SARS-CoV-2 replication-transcription complex.[43,54,55] SARS-CoV-2 mini replication-transcription complex harbors two Nsp13 molecules in distinct conformation (apo and RNA-bound). The 1B domain of the Nsp13 that constitutes CoV-RHIM-1 is essential for interacting with apo- and RNA-bound Nsp13 molecules in the replication-transcription complex.[54,55] The RNA binding channel of Nsp13 comprises domain 1B, Rec1A, and Rec2A and is critical for holding incoming RNA genome. Of note, studies on SARS-CoV-1 and other CoV Nsp13 suggested that alterations or mutations in Nsp13 abolish its helicase activity and restrict viral propagation.[59,60,82] Although the role of Nsp13 in SARS-CoV-2 replication and RNA genome unwinding has been described, its replication-independent functions have not been studied. Our cell death signaling, and biochemical studies indicate a critical role for the CoV-RHIM-1 and RNA-binding channel in Nsp13-mediated cell death. Also, intracellular RNA ligands and SC2-zRNAs further promoted Nsp13-mediated cell death. These observations suggest a replication-transcription complex-independent role of Nsp13 in modulating host responses, and the conformation of the RNA binding channel is critical in this case. Defective viral genomes (DVGs) generated during RNA virus replication are known to affect host innate immune responses.[83,84] DVGs are the source of Z-RNAs in IAV infection, and ZBP1 senses DVGs to trigger IAV-induced cell death.[27] Also, endogenous Z-RNA sensing by ZBP1 in physiological conditions triggers immunopathology.[75,76,85,86] Our

*in vitro* functional studies revealed a possible ZBP1-like function of Nsp13 to promote programmed cell death. Recent studies show that SARS-CoV-2 infection *in vitro* and infected patients generate DVGs associated with innate immune activation.[87–89] Nsp13 might act as a sensor when it is not an integral part of the replication-transcription complex, detect specific RNA ligands formed in infected cells, and trigger cell death like ZBP1. Perhaps, Nsp13 detects specific RNA patterns of the SARS-CoV-2 RNA genome or DVGs that might attain Z-RNA conformation to activate cell death. An intriguing question is why Nsp13 has evolved to promote cell death, unlike other viral RHIM proteins which inhibit cell death? We anticipate that SARS-CoV-2 mediated delayed type I IFN response limits ZBP1-RIPK3 signaling and exerts suboptimal cell death activation at an early stage of infection. Nsp13 might have evolved to trigger RHIM-dependent cell death at later stages of infection to promote virus spread. Nevertheless, future studies need to examine this question.

While this manuscript was in preparation, a new study reported that SARS-CoV-2 forms Z-RNAs in infected cells and activates ZBP1-RIPK3 signaling and cell death.[38] This work demonstrates that ZBP1-RIPK3 signaling promotes lung damage and inflammation during SARS-CoV-2 infection in mice. This study suggests the formation of Z-RNAs in SARS-CoV-2 infection, however, specific RNA genome regions of SARS-CoV-2 attaining Z-RNA conformation and their interaction with Z-nucleic acid binding domains (Zα domains) was unknown. Our stringent pipeline for identifying Z-RNA sequences led us to annotate high-propensity Z-RNA forming sequences in the SARS-CoV-2 genome (SC2-zRNAs). Our biochemical and real-time binding studies demonstrate the binding of SC2-zRNAs to purified Zα1Zα2 domains of human ZBP1 protein. These observations reveal SARS-CoV-2 RNA genome-derived Z-RNA ligands that might activate ZBP1 and Nsp13-mediated cell death. Our cell death experiments in Nsp13 expressing cells demonstrated that delivery of SC2-zRNAs into these cells increased Nsp13 mediated cell death, suggesting zRNAs' role in Nsp13 mediated cell death. However, we cannot exclude the possibility that the zRNA might induce cell death independent of Nsp13.

### Limitations of the study

Our study identified viral RHIMs in SARS-CoV-2 Nsp13 and other bat-originated pathogenic RNA viruses. Our experiments further characterized the mechanism of cell death activation by Nsp13. We established the role of Nsp13-mediated cell death during SARS-CoV-2 infection through ectopic expression studies. However, the conclusions of the SARS-CoV-2 virus experiments are limited due to the lack of Nsp13 mutant SARS-CoV-2, which lacks viral RHIMs. The generation of these mutants is challenging because Nsp13 is an essential part of the replication-transcription complex, and introducing substitutions in Nsp13 might adversely affect the replication and fitness of the SARS-CoV-2 virus. Our observations in this study also suggest that the SARS-CoV-2 genome consisted of Z-RNAs, and these Z-RNAs promoted Nsp13-mediated cell death in *in vitro* studies. The limitation of this study is demonstrating the interaction of Nsp13 with Z-RNAs and its downstream role in facilitating cell death. Also, the species-specific cell death regulation conclusions mainly compare only one bat-derived cell line with human cells, and perhaps the cell death regulation could be due to the tissue origin of the bat cells.

## RESOURCE AVAILABILITY

### Lead contact

Further information and requests for resources and reagents should be directed to and will be fulfilled by the lead contact, Sannula Kesavardhana (skesav@iisc.ac.in).

### Materials availability

All materials generated in this study are available from the lead contact.

### Data and code availability

- All data reported in this paper will be shared by the lead contact upon request.
- This paper does not report the original code.
- Any additional information required to reanalyze the data reported in this paper is available from the lead contact upon request.

## ACKNOWLEDGMENTS

We thank S.K. lab members for their critical comments. We are very grateful to Nevan Krogan, Margaret Soucheray, and Ujjwal Rathore from the University of California San Francisco for providing SARS-CoV-2, SARS-CoV, and MERS-CoV protein expression clones. We thank Paul G. Thomas from St. Jude Children's Research Hospital for the helpful discussions. This work was supported by funding from the Indian Council of Medical Research (2021-14148/CMB/ADHOC-BMS) (EMDR/SG/9/2023-2019), Department of Biotechnology (DBT) (BT/PR45145/COT/142/24/2022), Scheme for Transformational and Advanced Research in Sciences (STARS)-MoE (MoE-STARS/STARS-2/2023-0464), the Science and Engineering Research Board (SRG/2021/000632) (EEQ/2021/000274) and the Indian Institute of Science (IISc) Start-up grant. We acknowledge Viral BSL-3 Facility at CIDR, IISc supported by DBT-BIRAC and Crypto-Relief Foundation. S.M. is the recipient of the Prime Minister Research Fellowship (PMRF) scheme in India.

## AUTHOR CONTRIBUTIONS

S.K. conceptualized the study; S.M., D.J., A.A.D., S.N., and S.K. designed experiments, performed cell culture and biochemical experiments; S.K., K.B., and A.A.D. performed sequence and phylogenetic analysis; D.J. and S.K. performed Z-RNA mining and sequence analysis; D.J. and M.S. performed *in vitro* transcriptions, purification of Za protein, EMSA, and Octet binding studies; S.M, A.A.D., and M.A. performed imaging and DNA-PAINT studies; S.M., O.K., and A.A.D. performed SARS-CoV-2 infections and viral titer assays; S.T. assisted with SARS-CoV-2 infection experiments; M.G. helped with protein purification and DNA-PAINT experiments; A.K.A. performed molecular docking studies; S.M., D.J., A.A.D., and S.K. wrote the manuscript; M.G. and S.K. supervised the study; S.K. provided the guidance, and brought the funding; All the authors contributed in manuscript editing.

## DECLARATION OF INTERESTS

The authors declare no conflicts of interest.

## STAR★METHODS

Detailed methods are provided in the online version of this paper and include the following:

- KEY RESOURCES TABLE
- EXPERIMENTAL MODEL AND STUDY PARTICIPANT DETAILS
  - Cell culture

## SUPPLEMENTAL INFORMATION

Supplemental information can be found online at https://doi.org/10.1016/j.isci.2024.111444.

Received: September 22, 2023
Revised: January 6, 2024
Accepted: November 18, 2024
Published: November 20, 2024

## REFERENCES

1. Flerlage, T., Boyd, D.F., Meliopoulos, V., Thomas, P.G., and Schultz-Cherry, S. (2021). Influenza virus and SARS-CoV-2: pathogenesis and host responses in the respiratory tract. Nat. Rev. Microbiol. *19*, 425–441. https://doi.org/10.1038/s41579-021-00542-7.
2. Diamond, M.S., and Kanneganti, T.D. (2022). Innate immunity: the first line of defense against SARS-CoV-2. Nat. Immunol. *23*, 165–176. https://doi.org/10.1038/s41590-021-01091-0.
3. Balachandran, S., and Mocarski, E.S. (2021). Viral Z-RNA triggers ZBP1-dependent cell death. Curr. Opin. Virol. *51*, 134–140. https://doi.org/10.1016/j.coviro.2021.10.004.
4. Zhou, P., Yang, X.L., Wang, X.G., Hu, B., Zhang, L., Zhang, W., Si, H.R., Zhu, Y., Li, B., Huang, C.L., et al. (2020). A pneumonia outbreak associated with a new coronavirus of probable bat origin. Nature *579*, 270–273. https://doi.org/10.1038/s41586-020-2012-7.
5. Yang, X., Yu, Y., Xu, J., Shu, H., Xia, J., Liu, H., Wu, Y., Zhang, L., Yu, Z., Fang, M., et al. (2020). Clinical course and outcomes of critically ill patients with SARS-CoV-2 pneumonia in Wuhan, China: a single-centered, retrospective, observational study. Lancet Respir. Med. *8*, 475–481. https://doi.org/10.1016/S2213-2600(20)30079-5.
6. Nagaraja, S., Jain, D., and Kesavardhana, S. (2022). Inflammasome regulation in driving COVID-19 severity in humans and immune tolerance in bats. J. Leukoc. Biol. *111*, 497–508. https://doi.org/10.1002/JLB.4COVHR0221-093RR.
7. Garcia-Sastre, A. (2017). Ten Strategies of Interferon Evasion by Viruses. Cell Host Microbe *22*, 176–184. https://doi.org/10.1016/j.chom.2017.07.012.
8. Minkoff, J.M., and tenOever, B. (2023). Innate immune evasion strategies of SARS-CoV-2. Nat. Rev. Microbiol. *21*, 178–194. https://doi.org/10.1038/s41579-022-00839-1.
9. Thomas, P.G., Shubina, M., and Balachandran, S. (2023). ZBP1/DAI-Dependent Cell Death Pathways in Influenza A Virus Immunity and Pathogenesis. Curr. Top. Microbiol. Immunol. *442*, 41–63. https://doi.org/10.1007/82_2019_190.
10. Basavaraju, S., Mishra, S., Jindal, R., and Kesavardhana, S. (2022). Emerging Role of ZBP1 in Z-RNA Sensing, Influenza Virus-Induced Cell Death, and Pulmonary Inflammation. mBio *13*, e0040122. https://doi.org/10.1128/mbio.00401-22.
11. Kaiser, W.J., Upton, J.W., and Mocarski, E.S. (2013). Viral modulation of programmed necrosis. Curr. Opin. Virol. *3*, 296–306. https://doi.org/10.1016/j.coviro.2013.05.019.
12. Karki, R., Sharma, B.R., Tuladhar, S., Williams, E.P., Zalduondo, L., Samir, P., Zheng, M., Sundaram, B., Banoth, B., Malireddi, R.K.S., et al. (2021). Synergism of TNF-alpha and IFN-gamma Triggers Inflammatory Cell Death, Tissue Damage, and Mortality in SARS-CoV-2 Infection and Cytokine Shock Syndromes. Cell *184*, 149. https://doi.org/10.1016/j.cell.2020.11.025.
13. Kesavardhana, S., Malireddi, R.K.S., and Kanneganti, T.D. (2020). Caspases in Cell Death, Inflammation, and Pyroptosis. Annu. Rev. Immunol. *38*, 567–595. https://doi.org/10.1146/annurev-immunol-073119-095439.
14. Mompeán, M., Bozkurt, G., and Wu, H. (2019). Mimicry by a viral RHIM. EMBO Rep. *20*, e47433. https://doi.org/10.15252/embr.201847433.
15. Li, J., McQuade, T., Siemer, A.B., Napetschnig, J., Moriwaki, K., Hsiao, Y.S., Damko, E., Moquin, D., Walz, T., McDermott, A., et al. (2012). The RIP1/RIP3 necrosome forms a functional amyloid signaling complex required for programmed necrosis. Cell *150*, 339–350. https://doi.org/10.1016/j.cell.2012.06.019.
16. Sun, X., Yin, J., Starovasnik, M.A., Fairbrother, W.J., and Dixit, V.M. (2002). Identification of a novel homotypic interaction motif required for the phosphorylation of receptor-interacting protein (RIP) by RIP3. J. Biol. Chem. *277*, 9505–9511. https://doi.org/10.1074/jbc.M109488200.
17. Mandal, P., Berger, S.B., Pillay, S., Moriwaki, K., Huang, C., Guo, H., Lich, J.D., Finger, J., Kasparcova, V., Votta, B., et al. (2014). RIP3 induces apoptosis independent of pronecrotic kinase activity. Mol. Cell *56*, 481–495. https://doi.org/10.1016/j.molcel.2014.10.021.
18. Newton, K., Dugger, D.L., Wickliffe, K.E., Kapoor, N., de Almagro, M.C., Vucic, D., Komuves, L., Ferrando, R.E., French, D.M., Webster, J., et al. (2014). Activity of protein kinase RIPK3 determines whether cells die by necroptosis or apoptosis. Science *343*, 1357–1360. https://doi.org/10.1126/science.1249361.
19. Nogusa, S., Thapa, R.J., Dillon, C.P., Liedmann, S., Oguin, T.H., 3rd, Ingram, J.P., Rodriguez, D.A., Kosoff, R., Sharma, S., et al. (2016). RIPK3 Activates Parallel Pathways of MLKL-Driven Necroptosis and FADD-Mediated Apoptosis to Protect against Influenza A Virus. Cell Host Microbe *20*, 13–24. https://doi.org/10.1016/j.chom.2016.05.011.
20. Upton, J.W., Kaiser, W.J., and Mocarski, E.S. (2010). Virus inhibition of RIP3-dependent necrosis. Cell Host Microbe *7*, 302–313. https://doi.org/10.1016/j.chom.2010.03.006.
21. Upton, J.W., Kaiser, W.J., and Mocarski, E.S. (2012). DAI/ZBP1/DLM-1 complexes with RIP3 to mediate virus-induced programmed necrosis that is targeted by murine cytomegalovirus vIRA. Cell Host Microbe *11*, 290–297. https://doi.org/10.1016/j.chom.2012.01.016.
22. Kuriakose, T., Man, S.M., Malireddi, R.K.S., Karki, R., Kesavardhana, S., Place, D.E., Neale, G., Vogel, P., and Kanneganti, T.D. (2016). ZBP1/DAI is an innate sensor of influenza virus triggering the NLRP3 inflammasome and programmed cell death pathways. Sci. Immunol. *1*, aag2045. https://doi.org/10.1126/sciimmunol.aag2045.
23. Thapa, R.J., Ingram, J.P., Ragan, K.B., Nogusa, S., Boyd, D.F., Benitez, A.A., Sridharan, H., Kosoff, R., Shubina, M., Landsteiner, V.J., et al. (2016). DAI Senses Influenza A Virus Genomic RNA and Activates RIPK3-Dependent Cell Death. Cell Host Microbe *20*, 674–681. https://doi.org/10.1016/j.chom.2016.09.014.
24. Guo, H., Gilley, R.P., Fisher, A., Lane, R., Landsteiner, V.J., Ragan, K.B., Dovey, C.M., Carette, J.E., Upton, J.W., Mocarski, E.S., and Kaiser, W.J. (2018). Species-independent contribution of ZBP1/DAI/DLM-1-triggered

necroptosis in host defense against HSV1. Cell Death Dis. *9*, 816. https://doi.org/10.1038/s41419-018-0868-3.

25. Kesavardhana, S., Malireddi, R.K.S., Burton, A.R., Porter, S.N., Vogel, P., Pruett-Miller, S.M., and Kanneganti, T.D. (2020). The Zalpha2 domain of ZBP1 is a molecular switch regulating influenza-induced PANoptosis and perinatal lethality during development. J. Biol. Chem. *295*, 8325–8330. https://doi.org/10.1074/jbc.RA120.013752.
26. Wang, X., Li, Y., Liu, S., Yu, X., Li, L., Shi, C., He, W., Li, J., Xu, L., Hu, Z., et al. (2014). Direct activation of RIP3/MLKL-dependent necrosis by herpes simplex virus 1 (HSV-1) protein ICP6 triggers host antiviral defense. Proc. Natl. Acad. Sci. USA *111*, 15438–15443. https://doi.org/10.1073/pnas.1412767111.
27. Zhang, T., Yin, C., Boyd, D.F., Quarato, G., Ingram, J.P., Shubina, M., Ragan, K.B., Ishizuka, T., Crawford, J.C., Tummers, B., et al. (2020). Influenza Virus Z-RNAs Induce ZBP1-Mediated Necroptosis. Cell *180*, 1115. https://doi.org/10.1016/j.cell.2020.02.050.
28. Karki, R., and Kanneganti, T.D. (2023). PANoptosome signaling and therapeutic implications in infection: central role for ZBP1 to activate the inflammasome and PANoptosis. Curr. Opin. Immunol. *83*, 102348. https://doi.org/10.1016/j.coi.2023.102348.
29. Christgen, S., Zheng, M., Kesavardhana, S., Karki, R., Malireddi, R.K.S., Banoth, B., Place, D.E., Briard, B., Sharma, B.R., Tuladhar, S., et al. (2020). Identification of the PANoptosome: A Molecular Platform Triggering Pyroptosis, Apoptosis, and Necroptosis (PANoptosis). Front. Cell. Infect. Microbiol. *10*, 237. https://doi.org/10.3389/fcimb.2020.00237.
30. Kesavardhana, S., and Kanneganti, T.D. (2020). ZBP1: A STARGÅTE to decode the biology of Z-nucleic acids in disease. J. Exp. Med. *217*, e20200885. https://doi.org/10.1084/jem.20200885.
31. Guo, H., Omoto, S., Harris, P.A., Finger, J.N., Bertin, J., Gough, P.J., Kaiser, W.J., and Mocarski, E.S. (2015). Herpes simplex virus suppresses necroptosis in human cells. Cell Host Microbe *17*, 243–251. https://doi.org/10.1016/j.chom.2015.01.003.
32. Pham, C.L., Shanmugam, N., Strange, M., O'Carroll, A., Brown, J.W., Sierecki, E., Gambin, Y., Steain, M., and Sunde, M. (2019). Viral M45 and necroptosis-associated proteins form heteromeric amyloid assemblies. EMBO Rep. *20*, e46518. https://doi.org/10.15252/embr.201846518.
33. Steain, M., Baker, M.O.D.G., Pham, C.L.L., Shanmugam, N., Gambin, Y., Sierecki, E., McSharry, B.P., Avdic, S., Slobedman, B., Sunde, M., and Abendroth, A. (2020). Varicella zoster virus encodes a viral decoy RHIM to inhibit cell death. PLoS Pathog. *16*, e1008473. https://doi.org/10.1371/journal.ppat.1008473.
34. Huang, Z., Wu, S.Q., Liang, Y., Zhou, X., Chen, W., Li, L., Wu, J., Zhuang, Q., Chen, C., Li, J., et al. (2015). RIP1/RIP3 binding to HSV-1 ICP6 initiates necroptosis to restrict virus propagation in mice. Cell Host Microbe *17*, 229–242. https://doi.org/10.1016/j.chom.2015.01.002.
35. Koehler, H., Cotsmire, S., Langland, J., Kibler, K.V., Kalman, D., Upton, J.W., Mocarski, E.S., and Jacobs, B.L. (2017). Inhibition of DAI-dependent necroptosis by the Z-DNA binding domain of the vaccinia virus innate immune evasion protein, E3. Proc. Natl. Acad. Sci. USA *114*, 11506–11511. https://doi.org/10.1073/pnas.1700999114.
36. Koehler, H., Cotsmire, S., Zhang, T., Balachandran, S., Upton, J.W., Langland, J., Kalman, D., Jacobs, B.L., and Mocarski, E.S. (2021). Vaccinia virus E3 prevents sensing of Z-RNA to block ZBP1-dependent necroptosis. Cell Host Microbe *29*, 1266–1276.e5. https://doi.org/10.1016/j.chom.2021.05.009.
37. Li, S., Zhang, Y., Guan, Z., Li, H., Ye, M., Chen, X., Shen, J., Zhou, Y., Shi, Z.L., Zhou, P., and Peng, K. (2020). SARS-CoV-2 triggers inflammatory responses and cell death through caspase-8 activation. Signal Transduct. Targeted Ther. *5*, 235. https://doi.org/10.1038/s41392-020-00334-0.
38. Li, S., Zhang, Y., Guan, Z., Ye, M., Li, H., You, M., Zhou, Z., Zhang, C., Zhang, F., Lu, B., et al. (2023). SARS-CoV-2 Z-RNA activates the ZBP1-RIPK3 pathway to promote virus-induced inflammatory responses. Cell Res. *33*, 201–214. https://doi.org/10.1038/s41422-022-00775-y.
39. Eisenberg, D., and Jucker, M. (2012). The amyloid state of proteins in human diseases. Cell *148*, 1188–1203. https://doi.org/10.1016/j.cell.2012.02.022.
40. Kajava, A.V., Klopffleisch, K., Chen, S., and Hofmann, K. (2014). Evolutionary link between metazoan RHIM motif and prion-forming domain of fungal heterokaryon incompatibility factor HET-s/HET-s. Sci. Rep. *4*, 7436. https://doi.org/10.1038/srep07436.
41. Jiao, H., Wachsmuth, L., Kumari, S., Schwarzer, R., Lin, J., Eren, R.O., Fisher, A., Lane, R., Young, G.R., Kassiotis, G., et al. (2020). Z-nucleic-acid sensing triggers ZBP1-dependent necroptosis and inflammation. Nature *580*, 391–395. https://doi.org/10.1038/s41586-020-2129-8.
42. Newton, K., Wickliffe, K.E., Maltzman, A., Dugger, D.L., Strasser, A., Pham, V.C., Lill, J.R., Roose-Girma, M., Warming, S., Solon, M., et al. (2016). RIPK1 inhibits ZBP1-driven necroptosis during development. Nature *540*, 129–133. https://doi.org/10.1038/nature20559.
43. Newman, J.A., Douangamath, A., Yadzani, S., Yosaatmadja, Y., Aimon, A., Brandão-Neto, J., Dunnett, L., Gorrie-Stone, T., Skyner, R., Fearon, D., et al. (2021). Structure, mechanism and crystallographic fragment screening of the SARS-CoV-2 NSP13 helicase. Nat. Commun. *12*, 4848. https://doi.org/10.1038/s41467-021-25166-6.
44. Liu, C., Shi, W., Becker, S.T., Schatz, D.G., Liu, B., and Yang, Y. (2021). Structural basis of mismatch recognition by a SARS-CoV-2 proofreading enzyme. Science *373*, 1142–1146. https://doi.org/10.1126/science.abi9310.
45. Menachery, V.D., Yount, B.L., Jr., Debbink, K., Agnihothram, S., Gralinski, L.E., Plante, J.A., Graham, R.L., Scobey, T., Ge, X.Y., Donaldson, E.F., et al. (2015). A SARS-like cluster of circulating bat coronaviruses shows potential for human emergence. Nat. Med. *21*, 1508–1513. https://doi.org/10.1038/nm.3985.
46. Cui, J., Li, F., and Shi, Z.L. (2019). Origin and evolution of pathogenic coronaviruses. Nat. Rev. Microbiol. *17*, 181–192. https://doi.org/10.1038/s41579-018-0118-9.
47. Irving, A.T., Ahn, M., Goh, G., Anderson, D.E., and Wang, L.F. (2021). Lessons from the host defences of bats, a unique viral reservoir. Nature *589*, 363–370. https://doi.org/10.1038/s41586-020-03128-0.
48. Mandl, J.N., Ahmed, R., Barreiro, L.B., Daszak, P., Epstein, J.H., Virgin, H.W., and Feinberg, M.B. (2015). Reservoir host immune responses to emerging zoonotic viruses. Cell *160*, 20–35. https://doi.org/10.1016/j.cell.2014.12.003.
49. Pavlovich, S.S., Lovett, S.P., Koroleva, G., Guito, J.C., Arnold, C.E., Nagle, E.R., Kulcsar, K., Lee, A., Thibaud-Nissen, F., Hume, A.J., et al. (2018). The Egyptian Rousette Genome Reveals Unexpected Features of Bat Antiviral Immunity. Cell *173*, 1098–1110.e18. https://doi.org/10.1016/j.cell.2018.03.070.
50. Zhang, G., Cowled, C., Shi, Z., Huang, Z., Bishop-Lilly, K.A., Fang, X., Wynne, J.W., Xiong, Z., Baker, M.L., Zhao, W., et al. (2013). Comparative analysis of bat genomes provides insight into the evolution of flight and immunity. Science *339*, 456–460. https://doi.org/10.1126/science.1230835.
51. Dondelinger, Y., Hulpiau, P., Saeys, Y., Bertrand, M.J.M., and Vandenabeele, P. (2016). An evolutionary perspective on the necroptotic pathway. Trends Cell Biol. *26*, 721–732. https://doi.org/10.1016/j.tcb.2016.06.004.
52. Irving, A.T., Zhang, Q., Kong, P.S., Luko, K., Rozario, P., Wen, M., Zhu, F., Zhou, P., Ng, J.H.J., Sobota, R.M., and Wang, L.F. (2020). Interferon Regulatory Factors IRF1 and IRF7 Directly Regulate Gene Expression in Bats in Response to Viral Infection. Cell Rep. *33*, 108345. https://doi.org/10.1016/j.celrep.2020.108345.
53. Chen, J., Malone, B., Llewellyn, E., Grasso, M., Shelton, P.M.M., Olinares, P.D.B., Maruthi, K., Eng, E.T., Vatandaslar, H., Chait, B.T., et al. (2020). Structural Basis for Helicase-Polymerase Coupling in the

SARS-CoV-2 Replication-Transcription Complex. Cell *182*, 1560–1573.e13. https://doi.org/10.1016/j.cell.2020.07.033.

54. Yan, L., Zhang, Y., Ge, J., Zheng, L., Gao, Y., Wang, T., Jia, Z., Wang, H., Huang, Y., Li, M., et al. (2020). Architecture of a SARS-CoV-2 mini replication and transcription complex. Nat. Commun. *11*, 5874. https://doi.org/10.1038/s41467-020-19770-1.

55. Chen, J., Wang, Q., Malone, B., Llewellyn, E., Pechersky, Y., Maruthi, K., Eng, E.T., Perry, J.K., Campbell, E.A., Shaw, D.E., and Darst, S.A. (2022). Ensemble cryo-EM reveals conformational states of the nsp13 helicase in the SARS-CoV-2 helicase replication-transcription complex. Nat. Struct. Mol. Biol. *29*, 250–260. https://doi.org/10.1038/s41594-022-00734-6.

56. Naderi, S., Chen, P.E., Murall, C.L., Poujol, R., Kraemer, S., Pickering, B.S., Sagan, S.M., and Shapiro, B.J. (2023). Zooanthroponotic transmission of SARS-CoV-2 and host-specific viral mutations revealed by genome-wide phylogenetic analysis. Elife *12*, e83685. https://doi.org/10.7554/eLife.83685.

57. Garvin, M.R., T Prates, E., Pavicic, M., Jones, P., Amos, B.K., Geiger, A., Shah, M.B., Streich, J., Felipe Machado Gazolla, J.G., Kainer, D., et al. (2020). Potentially adaptive SARS-CoV-2 mutations discovered with novel spatiotemporal and explainable AI models. Genome Biol. *21*, 304. https://doi.org/10.1186/s13059-020-02191-0.

58. Grimes, S.L., Choi, Y.J., Banerjee, A., Small, G., Anderson-Daniels, J., Gribble, J., Pruijssers, A.J., Agostini, M.L., Abu-Shmais, A., Lu, X., et al. (2023). A mutation in the coronavirus nsp13-helicase impairs enzymatic activity and confers partial remdesivir resistance. mBio *14*, e0106023. https://doi.org/10.1128/mbio.01060-23.

59. Fang, S., Chen, B., Tay, F.P.L., Ng, B.S., and Liu, D.X. (2007). An arginine-to-proline mutation in a domain with undefined functions within the helicase protein (Nsp13) is lethal to the coronavirus infectious bronchitis virus in cultured cells. Virology *358*, 136–147. https://doi.org/10.1016/j.virol.2006.08.020.

60. Zhang, R., Li, Y., Cowley, T.J., Steinbrenner, A.D., Phillips, J.M., Yount, B.L., Baric, R.S., and Weiss, S.R. (2015). The nsp1, nsp13, and M proteins contribute to the hepatotropism of murine coronavirus JHM.WU. J. Virol. *89*, 3598–3609. https://doi.org/10.1128/JVI.03535-14.

61. Yue, K., Yao, B., Shi, Y., Yang, Y., Qian, Z., Ci, Y., and Shi, L. (2022). The stalk domain of SARS-CoV-2 NSP13 is essential for its helicase activity. Biochem. Biophys. Res. Commun. *601*, 129–136. https://doi.org/10.1016/j.bbrc.2022.02.068.

62. Sonnleitner, S.T., Prelog, M., Sonnleitner, S., Hinterbichler, E., Halbfurter, H., Kopecky, D.B.C., Almanzar, G., Koblmüller, S., Sturmbauer, C., Feist, L., et al. (2022). Cumulative SARS-CoV-2 mutations and corresponding changes in immunity in an immunocompromised patient indicate viral evolution within the host. Nat. Commun. *13*, 2560. https://doi.org/10.1038/s41467-022-30163-4.

63. Mompean, M., Li, W., Li, J., Laage, S., Siemer, A.B., Bozkurt, G., Wu, H., and McDermott, A.E. (2018). The Structure of the Necrosome RIPK1-RIPK3 Core, a Human Hetero-Amyloid Signaling Complex. Cell *173*, 1244–1253. https://doi.org/10.1016/j.cell.2018.03.032.

64. Cho, Y.S., Challa, S., Moquin, D., Genga, R., Ray, T.D., Guildford, M., and Chan, F.K.M. (2009). Phosphorylation-driven assembly of the RIP1-RIP3 complex regulates programmed necrosis and virus-induced inflammation. Cell *137*, 1112–1123. https://doi.org/10.1016/j.cell.2009.05.037.

65. Weinlich, R., Oberst, A., Beere, H.M., and Green, D.R. (2017). Necroptosis in development, inflammation and disease. Nat. Rev. Mol. Cell Biol. *18*, 127–136. https://doi.org/10.1038/nrm.2016.149.

66. Chen, X., Zhu, R., Zhong, J., Ying, Y., Wang, W., Cao, Y., Cai, H., Li, X., Shuai, J., and Han, J. (2022). Mosaic composition of RIP1-RIP3 signalling hub and its role in regulating cell death. Nat. Cell Biol. *24*, 471–482. https://doi.org/10.1038/s41556-022-00854-7.

67. Zhang, T., Yin, C., Fedorov, A., Qiao, L., Bao, H., Beknazarov, N., Wang, S., Gautam, A., Williams, R.M., Crawford, J.C., et al. (2022). ADAR1 masks the cancer immunotherapeutic promise of ZBP1-driven necroptosis. Nature *606*, 594–602. https://doi.org/10.1038/s41586-022-04753-7.

68. Kesavardhana, S., Kuriakose, T., Guy, C.S., Samir, P., Malireddi, R.K.S., Mishra, A., and Kanneganti, T.D. (2017). ZBP1/DAI ubiquitination and sensing of influenza vRNPs activate programmed cell death. J. Exp. Med. *214*, 2217–2229. https://doi.org/10.1084/jem.20170550.

69. Karki, R., Lee, S., Mall, R., Pandian, N., Wang, Y., Sharma, B.R., Malireddi, R.S., Yang, D., Trifkovic, S., Steele, J.A., et al. (2022). ZBP1-dependent inflammatory cell death, PANoptosis, and cytokine storm disrupt IFN therapeutic efficacy during coronavirus infection. Sci. Immunol. *7*, eabo6294. https://doi.org/10.1126/sciimmunol.abo6294.

70. Laurent, P., Yang, C., Rendeiro, A.F., Nilsson-Payant, B.E., Carrau, L., Chandar, V., Bram, Y., tenOever, B.R., Elemento, O., Ivashkiv, L.B., et al. (2022). Sensing of SARS-CoV-2 by pDCs and their subsequent production of IFN-I contribute to macrophage-induced cytokine storm during COVID-19. Sci. Immunol. *7*, eadd4906. https://doi.org/10.1126/sciimmunol.add4906.

71. Wong, L.Y.R., and Perlman, S. (2022). Immune dysregulation and immunopathology induced by SARS-CoV-2 and related coronaviruses - are we our own worst enemy? Nat. Rev. Immunol. *22*, 47–56. https://doi.org/10.1038/s41577-021-00656-2.

72. DeAntoneo, C., Herbert, A., and Balachandran, S. (2023). Z-form nucleic acid-binding protein 1 (ZBP1) as a sensor of viral and cellular Z-RNAs: walking the razor's edge. Curr. Opin. Immunol. *83*, 102347. https://doi.org/10.1016/j.coi.2023.102347.

73. Herbert, A., Karapetyan, S., Poptsova, M., Vasquez, K.M., Vicens, Q., and Vögeli, B. (2021). Special Issue: A, B and Z: The Structure, Function and Genetics of Z-DNA and Z-RNA. Int. J. Mol. Sci. *22*, 7686. https://doi.org/10.3390/ijms22147686.

74. Maelfait, J., and Rehwinkel, J. (2023). The Z-nucleic acid sensor ZBP1 in health and disease. J. Exp. Med. *220*, e20221156. https://doi.org/10.1084/jem.20221156.

75. Tang, Q., Rigby, R.E., Young, G.R., Hvidt, A.K., Davis, T., Tan, T.K., Bridgeman, A., Townsend, A.R., Kassiotis, G., and Rehwinkel, J. (2021). Adenosine-to-inosine editing of endogenous Z-form RNA by the deaminase ADAR1 prevents spontaneous MAVS-dependent type I interferon responses. Immunity *54*, 1961. https://doi.org/10.1016/j.immuni.2021.08.011.

76. de Reuver, R., Verdonck, S., Dierick, E., Nemegeer, J., Hessmann, E., Ahmad, S., Jans, M., Blancke, G., Van Nieuwerburgh, F., Botzki, A., et al. (2022). ADAR1 prevents autoinflammation by suppressing spontaneous ZBP1 activation. Nature *607*, 784–789. https://doi.org/10.1038/s41586-022-04974-w.

77. Huston, N.C., Wan, H., Strine, M.S., de Cesaris Araujo Tavares, R., Wilen, C.B., and Pyle, A.M. (2021). Comprehensive *in vivo* secondary structure of the SARS-CoV-2 genome reveals novel regulatory motifs and mechanisms. Mol. Cell *81*, 584. https://doi.org/10.1016/j.molcel.2020.12.041.

78. Sun, L., Li, P., Ju, X., Rao, J., Huang, W., Ren, L., Zhang, S., Xiong, T., Xu, K., Zhou, X., et al. (2021). In vivo structural characterization of the SARS-CoV-2 RNA genome identifies host proteins vulnerable to repurposed drugs. Cell *184*, 1865. https://doi.org/10.1016/j.cell.2021.02.008.

79. Lan, T.C.T., Allan, M.F., Malsick, L.E., Woo, J.Z., Zhu, C., Zhang, F., Khandwala, S., Nyeo, S.S.Y., Sun, Y., Guo, J.U., et al. (2022). Secondary structural ensembles of the SARS-CoV-2 RNA genome in infected cells. Nat. Commun. *13*, 1128. https://doi.org/10.1038/s41467-022-28603-2.

80. Balasubramaniyam, T., Ishizuka, T., Xiao, C.D., Bao, H.L., and Xu, Y. (2018). 2'-O-Methyl-8-methylguanosine as a Z-Form RNA Stabilizer for Structural and Functional Study of Z-RNA. Molecules *23*, 2572. https://doi.org/10.3390/molecules23102572.

81. Herbert, A., and Poptsova, M. (2022). Z-RNA and the Flipside of the SARS Nsp13 Helicase: Is There a Role for Flipons in Coronavirus-Induced Pathology? Front. Immunol. *13*, 912717. https://doi.org/10.3389/fimmu.2022.912717.

82. Seybert, A., Posthuma, C.C., van Dinten, L.C., Snijder, E.J., Gorbalenya, A.E., and Ziebuhr, J. (2005). A complex zinc finger controls the enzymatic activities of nidovirus helicases. J. Virol. *79*, 696–704. https://doi.org/10.1128/JVI.79.2.696-704.2005.

83. Genoyer, E., and López, C.B. (2019). The Impact of Defective Viruses on Infection and Immunity. Annu. Rev. Virol. *6*, 547–566. https://doi.org/10.1146/annurev-virology-092818-015652.

84. Vignuzzi, M., and López, C.B. (2019). Defective viral genomes are key drivers of the virus-host interaction. Nat. Microbiol. *4*, 1075–1087. https://doi.org/10.1038/s41564-019-0465-y.

85. Hubbard, N.W., Ames, J.M., Maurano, M., Chu, L.H., Somfleth, K.Y., Gokhale, N.S., Werner, M., Snyder, J.M., Lichauco, K., Savan, R., et al. (2022). ADAR1 mutation causes ZBP1-dependent immunopathology. Nature *607*, 769–775. https://doi.org/10.1038/s41586-022-04896-7.

86. Karki, R., Sundaram, B., Sharma, B.R., Lee, S., Malireddi, R.K.S., Nguyen, L.N., Christgen, S., Zheng, M., Wang, Y., Samir, P., et al. (2021). ADAR1 restricts ZBP1-mediated immune response and PANoptosis to promote tumorigenesis. Cell Rep. *37*, 109858. https://doi.org/10.1016/j.celrep.2021.109858.

87. Girgis, S., Xu, Z., Oikonomopoulos, S., Fedorova, A.D., Tchesnokov, E.P., Gordon, C.J., Schmeing, T.M., Götte, M., Sonenberg, N., Baranov, P.V., et al. (2022). Evolution of naturally arising SARS-CoV-2 defective interfering particles. Commun. Biol. *5*, 1140. https://doi.org/10.1038/s42003-022-04058-5.

88. Zhou, T., Gilliam, N.J., Li, S., Spandau, S., Osborn, R.M., Connor, S., Anderson, C.S., Mariani, T.J., Thakar, J., Dewhurst, S., et al. (2023). Generation and Functional Analysis of Defective Viral Genomes during SARS-CoV-2 Infection. mBio *14*, e0025023. https://doi.org/10.1128/mbio.00250-23.

89. Xiao, Y., Lidsky, P.V., Shirogane, Y., Aviner, R., Wu, C.T., Li, W., Zheng, W., Talbot, D., Catching, A., Doitsh, G., et al. (2021). A defective viral genome strategy elicits broad protective immunity against respiratory viruses. Cell *184*, 6037. https://doi.org/10.1016/j.cell.2021.11.023.

90. Khatun, O., Sharma, M., Narayan, R., and Tripathi, S. (2023). SARS-CoV-2 ORF6 protein targets TRIM25 for proteasomal degradation to diminish K63-linked RIG-I ubiquitination and type-I interferon induction. Cell. Mol. Life Sci. *80*, 364. https://doi.org/10.1007/s00018-023-05011-3.

91. Gordon, D.E., Jang, G.M., Bouhaddou, M., Xu, J., Obernier, K., White, K.M., O'Meara, M.J., Rezelj, V.V., Guo, J.Z., Swaney, D.L., et al. (2020). A SARS-CoV-2 protein interaction map reveals targets for drug repurposing. Nature *583*, 459–468. https://doi.org/10.1038/s41586-020-2286-9.

92. Seo, J., Lee, E.W., Sung, H., Seong, D., Dondelinger, Y., Shin, J., Jeong, M., Lee, H.K., Kim, J.H., Han, S.Y., et al. (2016). CHIP controls necroptosis through ubiquitylation- and lysosome-dependent degradation of RIPK3. Nat. Cell Biol. *18*, 291–302. https://doi.org/10.1038/ncb3314.

93. Sanjana, N.E., Shalem, O., and Zhang, F. (2014). Improved vectors and genome-wide libraries for CRISPR screening. Nat. Methods *11*, 783–784. https://doi.org/10.1038/nmeth.3047.

94. Stewart, S.A., Dykxhoorn, D.M., Palliser, D., Mizuno, H., Yu, E.Y., An, D.S., Sabatini, D.M., Chen, I.S.Y., Hahn, W.C., Sharp, P.A., et al. (2003). Lentivirus-delivered stable gene silencing by RNAi in primary cells. RNA *9*, 493–501. https://doi.org/10.1261/rna.2192803.

95. Dereeper, A., Guignon, V., Blanc, G., Audic, S., Buffet, S., Chevenet, F., Dufayard, J.F., Guindon, S., Lefort, V., Lescot, M., et al. (2008). Phylogeny.fr: robust phylogenetic analysis for the non-specialist. Nucleic Acids Res. *36*, W465–W469. https://doi.org/10.1093/nar/gkn180.

96. Kumar, S., Stecher, G., Li, M., Knyaz, C., and Tamura, K. (2018). MEGA X: Molecular Evolutionary Genetics Analysis across Computing Platforms. Mol. Biol. Evol. *35*, 1547–1549. https://doi.org/10.1093/molbev/msy096.

97. Pettersen, E.F., Goddard, T.D., Huang, C.C., Couch, G.S., Greenblatt, D.M., Meng, E.C., and Ferrin, T.E. (2004). UCSF Chimera–a visualization system for exploratory research and analysis. J. Comput. Chem. *25*, 1605–1612. https://doi.org/10.1002/jcc.20084.

98. Dominguez, C., Boelens, R., and Bonvin, A.M.J.J. (2003). HADDOCK: a protein-protein docking approach based on biochemical or biophysical information. J. Am. Chem. Soc. *125*, 1731–1737. https://doi.org/10.1021/ja026939x.

99. van Zundert, G.C.P., Rodrigues, J.P.G.L.M., Trellet, M., Schmitz, C., Kastritis, P.L., Karaca, E., Melquiond, A.S.J., van Dijk, M., de Vries, S.J., and Bonvin, A.M.J.J. (2016). The HADDOCK2.2 Web Server: User-Friendly Integrative Modeling of Biomolecular Complexes. J. Mol. Biol. *428*, 720–725. https://doi.org/10.1016/j.jmb.2015.09.014.

100. Huang, J., and MacKerell, A.D., Jr. (2013). CHARMM36 all-atom additive protein force field: validation based on comparison to NMR data. J. Comput. Chem. *34*, 2135–2145. https://doi.org/10.1002/jcc.23354.

101. Yan, Y., Tao, H., He, J., and Huang, S.Y. (2020). The HDOCK server for integrated protein-protein docking. Nat. Protoc. *15*, 1829–1852. https://doi.org/10.1038/s41596-020-0312-x.

## STAR★METHODS

### KEY RESOURCES TABLE

| REAGENT or RESOURCE | SOURCE | IDENTIFIER |
|---|---|---|
| **Antibodies** | | |
| Mouse monoclonal Anti-ZBP1 (Zippy-1) | AdipoGen Life Sciences | AG-20B-0010-C100 |
| Mouse monoclonal Anti-ZBP1 (H-9) | Santa Cruz Biotechnology | sc-271483; RRID:AB_10650130 |
| Mouse monoclonal Anti-Strep-Tag | Qiagen | 34850; RRID:AB_2810987 |
| Rabbit monoclonal Anti-MLKL (Mouse-specific) | Cell Signaling Technology | 37705; RRID:AB_2799118 |
| Rabbit monoclonal Anti-MLKL (Human-specific) | Cell Signaling Technology | 14993; RRID:AB_2721822 |
| Rabbit monoclonal Anti-p-MLKL(Mouse-specific) | Cell Signaling Technology | 37333; RRID:AB_2799112 |
| Rabbit monoclonal Anti-p-MLKL(Human-specific) | Cell Signaling Technology | 91689; RRID:AB_2895044 |
| Rabbit monoclonal Anti-RIPK3 (Mouse-specific) | Cell Signaling Technology | 95702; RRID:AB_2721823 |
| Rabbit monoclonal Anti-RIPK3 (Human-specific) | Cell Signaling Technology | 10188; RRID:AB_2904619 |
| Rabbit polyclonal Anti-Caspase-3 | Cell Signaling Technology | 9662; RRID:AB_331439 |
| Rabbit monoclonal Anti-RIPK1 | Cell Signaling Technology | 3493; RRID:AB_2305314 |
| Mouse monoclonal Anti-SARS-CoV-2 N protein | Cell Signaling Technology | 33717; RRID:AB_2941972 |
| Mouse monoclonal Anti-GAPDH | Invitrogen | MA5-15738; RRID:AB_2537653 |
| Rabbit polyclonal Anti-IAV Nucleoprotein | Invitrogen | PA5-32242; RRID:AB_2549715 |
| Mouse monoclonal Anti-HA Tag | Invitrogen | 26183; RRID:AB_2533049 |
| Mouse monoclonal Anti-Flag Tag | Invitrogen | MA1-91878; RRID:AB_2537619 |
| Peroxidase AffiniPure™ Goat Anti-Rabbit IgG | Jackson ImmunoResearch | 111-035-047; RRID:AB_2337940 |
| Peroxidase AffiniPure™ Rabbit Anti-Mouse IgG | Jackson ImmunoResearch | 315-035-047; RRID:AB_2340068 |
| Goat anti-Mouse IgG (H+L) Cross-Adsorbed Secondary Antibody, Alexa Fluor™ 568 | Invitrogen | A-11004; RRID: AB_2534072 |
| Rabbit polyclonal Anti-GFP | Invitrogen | A-11122; RRID: AB_221569 |
| **Bacterial and virus strains** | | |
| SARS-CoV-2 Hong Kong/VM20001061/2020 | BEI Resources | NR-52282 |
| Influenza A virus (A/WSN/1933) | Paul G. Thomas Lab (St. Jude Children's Research Hospital) | N/A |
| Rosetta (DE3) | Professor Balasubramanian Gopal Lab (MBU,IISc) | N/A |
| **Chemicals, peptides, and recombinant proteins** | | |
| EcoRI-HF Restriction Enzyme | NEB | R3101S |
| BamHI-HF Restriction Enzyme | NEB | R3136S |
| DMEM, high glucose, pyruvate | ThermoFisher Scientific | 11995040 |
| Antibiotic-Antimycotic | ThermoFisher Scientific | 15240062 |
| FBS | ThermoFisher Scientific | 10270106 |
| Non-essential amino acids | ThermoFisher Scientific | 11140-050 |

(*Continued on next page*)

*Continued*

| REAGENT or RESOURCE | SOURCE | IDENTIFIER |
|---|---|---|
| EMEM | Lonza Bioscience | 12611F |
| Xfect Transfection Reagent | TakaraBio | 631318 |
| Lipofectamine 2000 | ThermoFisher Scientific | 11668-019 |
| Opti-MEM (Reduced serum media) | ThermoFisher Scientific | 31985070 |
| SMAC mimetic SM-164 | MedChemExpress | HY-15989 |
| Recombinant human TNF-α | Abclonal | RP00001 |
| Z-VAD(OMe)-FMK | Cayman Chemical | 14463 |
| MLKL Inhibitor (GW806742X) | Sigma Aldrich | SML1990 |
| Leptomycin-B | Sigma-Aldrich | L2913 |
| IFN-β | Abclonal | RP01076 |
| CBL0137 19110 | Cayman Chemicals | 19110 |
| DMEM, high glucose, without L-glutamine and sodium pyruvate | Sigma Aldrich | D6171 |
| Polybrene | Sigma Aldrich | TR-1003-G |
| Blasticidin S HCl, powder | ThermoFisher Scientific | R21001 |
| Puromycin dihydrochloride | Sigma-Aldrich | P8833 |
| SYTOX Green Nucleic Acid Stain | ThermoFisher Scientific | S7020 |
| Caspase-3/7 Green Dye | Sartorius | 4440 |
| Avicel | Dupont | RC-591 |
| Paraformaldehyde solution 4% in PBS | ChemCruz | sc-281692 |
| Crystal Violet | Sigma Aldrich | C0775 |
| Protein A/G PLUS-Agarose | Santa Cruz Biotechnology | 38221990 |
| BSA | GBiosciences | RC1021 |
| Pierce Premium Grade DSP | ThermoFisher Scientific | PG82081 |
| Immobilon Forte Western HRP substrate | Millipore | WBLUF0500 |
| Paraformaldehyde | Electron Microscopy Sciences | 15710 |
| Ni-NTA beads | GBiosciences | 786-940 |
| Poly I:C | Sigma Aldrich | P1530 |
| Sulfo-NHS reagents | Sigma Aldrich | 119616-38-5 |
| **Critical commercial assays** | | |
| HiScribe T7 High Yield RNA Synthesis Kit | NEB | E2040S |
| **Experimental models: Cell lines** | | |
| A549 (Human lung carcinoma) | National Centre for Cell Science (NCCS) cell repository | N/A |
| A549-ACE2 | Shashank Tripathi Lab[90] | N/A |
| HT-29 (Human colorectal adenocarcinoma) | National Centre for Cell Science (NCCS) cell repository | N/A |
| HCT-116 (Human colorectal adenocarcinoma) | National Centre for Cell Science (NCCS) cell repository | N/A |
| HEK-293T (Human embryonic kidney) | National Centre for Cell Science (NCCS) cell repository | N/A |
| Tb1 Lu (*T.brasiliensis* lung epithelial cell line (bat cell line)) | National Centre for Cell Science (NCCS) cell repository | N/A |
| MDCK (Madin-Darby canine kidney) | National Centre for Cell Science (NCCS) cell repository | N/A |
| L929 (Mouse lung fibroblast) | National Centre for Cell Science (NCCS) cell repository | N/A |
| L929 *Zbp1*$^{-/-}$ Cells | This paper | N/A |
| Vero-E6 | National Centre for Cell Science (NCCS) cell repository | N/A |

(*Continued on next page*)

*Continued*

| REAGENT or RESOURCE | SOURCE | IDENTIFIER |
|---|---|---|
| Oligonucleotides | | |
| SC2_ZRNA_1_R1-AGGAGGAAAAAATC CTTTGCCCGAAAATAAGTGAGTATGT AGCCATACTCCACTCACCTATAGTG AGTCGTATTAGGATCC | This Paper | N/A |
| SC2_ZRNA_1_R2- TGGTGGTAAAAATCC TTTGCCCGAAAAATAGTGACCACACTG GTAATTACCAGTGTACTCACTAGCCTA TAGTGAGTCGTATTAGGATCC | This Paper | N/A |
| SC2_ZRNA_1_R3- AGAGAGAAAAAAT CCTTTGCCCGAAAACATGCTTATGTT TCACAAACATCACCTATAGTGAGTC GTATTAGGATCC | This Paper | N/A |
| SC2_ZRNA_1_R4- GTGTGTGTAAAAATC CTTTGCCCGAAAAAACAGAACACACAC ACTTAGATGAACCTGTTTGCGCATCTGT TACCTATAGTGAGTCGTATTAGGATCC | This Paper | N/A |
| SC2_ZRNA_1_R5- GAAGAAGAAAAATC CTTTGCCCGAAAACTGTACTCAATTGA GTTGAGTACAGCCCTATAGTGAGTCG TATTAGGATCC | This Paper | N/A |
| SC2_ZRNA_1_R6- TGTTGTTAAAAATCC TTTGCCCGAAAATCACACCCGGACG AAACCTAGATGTGCCCTATAGTGAGT CGTATTAGGATCC | This Paper | N/A |
| PC_ZRNA_1_M2- GGTTGGTAAAAATCC TTTGCCCGAAAAACGCGCGCGCGAAA ACGCGCGCGCCCTATAGTGAGTCGTA TTAGGATCC | This Paper | N/A |
| Recombinant DNA | | |
| pLVX-EF1alpha-SARS-CoV-2-Nsp13-2xStrep-IRES-Puro | Nevan Krogan Lab[91] | N/A |
| pLVX-EF1alpha-SARS-CoV-Nsp13-2xStrep-IRES-Puro | Nevan Krogan Lab[91] | N/A |
| pLVX-EF1alpha-MERS-Nsp13-2xStrep-IRES-Puro | Nevan Krogan Lab[91] | N/A |
| pLVX-EF1alpha-eGFP-2xStrep-IRES-Puro | Nevan Krogan Lab[91] | N/A |
| pLVX-EF1alpha-ZBP1-HA-IRES-Puro | This Paper | N/A |
| pLVX-EF1alpha-ZBP1-RHIM-Mut-HA-IRES-Puro | This Paper | N/A |
| pLVX-EF1alpha-ZBP1-dTomato-IRES-Puro | This Paper | N/A |
| pLVX-EF1alpha-SARS-CoV-2-Nsp13-Tet-Mut-2xStrep-IRES-Puro | This Paper | N/A |
| pLVX-EF1alpha-SARS-CoV-2-Δ1B Rec1A Rec2A-Nsp13-2xStrep-IRES-Puro | This Paper | N/A |
| pLVX-EF1alpha-SARS-CoV-2-Δ1B-Nsp13-2xStrep-IRES-Puro | This Paper | N/A |
| pLVX-EF1alpha-SARS-CoV-2-Δ1B Rec1A Rec2A -Nsp13-2xStrep-IRES-Puro | This Paper | N/A |
| pLVX-EF1alpha-SARS-CoV-2-ΔZBD-S-1B-Nsp13-2xStrep-IRES-Puro | This Paper | N/A |
| pLVX-EF1alpha-SARS-CoV-2-ΔZBD-S-Nsp13-2xStrep-IRES-Puro | This Paper | N/A |

(*Continued on next page*)

*Continued*

| REAGENT or RESOURCE | SOURCE | IDENTIFIER |
|---|---|---|
| pLVX-EF1alpha-SARS-CoV-2-ΔZBD-Nsp13-2xStrep-IRES-Puro | This Paper | N/A |
| pcDNA3-HA-RIPK3 | Seo et al.[92] | 78804; Addgene plasmid |
| pcDNA3-FLAG-RIPK1 | Seo et al.[92] | 78842; Addgene plasmid |
| pCMV-Human-ZBP1 cDNA | Sino Biological | HG19385-UT |
| pNIC-ZB-ZBP1-Zα1Zα2 | This Paper | N/A |
| LentiCas9-Blast | Sanjana et al.[93] | 52962; Addgene plasmid |
| psPAX2 | Didier Trono Lab | 12260; Addgene Plasmid |
| pMD2.G | Didier Trono Lab | 12259; Addgene Plasmid |
| pCMV-VSVG | Stewart et al.[94] | 8454; Addgene Plasmid |
| **Software and algorithms** | | |
| PhyML 3.1/3.0aLRT | Dereeper, A et al.[95] | http://www.phylogeny.fr/one_task.cgi?workflow_id=b02e40313c3ca8c0eb7cffafce3c2d6a&tab_index=1 |
| Clustal Omega MSA Tool | EMBL-EBI | https://www.ebi.ac.uk/jdispatcher/msa/clustalo |
| MEGA-X | Kumar, Sudhir et al.[96] | https://www.megasoftware.net/ |
| Chimera 1.14 or ChimeraX 1.4 | Pettersen, Eric F et al.[97] | https://www.cgl.ucsf.edu/chimera/download.html |
| GraphPad Prism 9.0 software | GraphPad | https://www.graphpad.com/scientific-software/prism/ |
| ImageJ | NIH | https://imagej.nih.gov/ij/ |
| B DNA Motif Search Tool (nBMST) | NIH | https://nonb-abcc.ncifcrf.gov/apps/nBMST/default/ |
| RNAfold | Mathew's lab | https://rna.urmc.rochester.edu/index.html |
| Microsatellite Repeat Finder | Dr. Joseba Bikandi | http://insilico.ehu.es/mini_tools/microsatellites/ |
| **Other** | | |
| IncuCyte S3 Live-Cell Analysis System | Sartorius | |
| Image Quant LAS500 or Image Quant 800 | Cytiva, Amersham | |
| Olympus FV 300 Confocal Microscope system | Olympus | |
| Octet RED96 System | Sartorius | |
| Nikon Ti2 Eclipse Microscope | Nikon | |
| **Deposited data** | | |
| Uncropped immunoblot data images | | https://data.mendeley.com/preview/rn5mmgky9r?a=04e1cfdd-12a3-4ded-8c18-04c76f71e979 https://doi.org/10.17632/rn5mmgky9r.1 |

## EXPERIMENTAL MODEL AND STUDY PARTICIPANT DETAILS

### Cell culture

All the cell lines used in this study (A549, HT-29, HCT-116, L929, HEK-293T, MDCK, A549-ACE2 and Vero-E6) were cultured at 37°C and 5% $CO_2$ inside humidified incubators. The cells were maintained in DMEM growth medium supplemented with 10% v/v FBS, antibiotic-antimycotic, and non-essential amino acids (NEAA). Tb1 Lu cells were cultures in EMEM growth medium with the conditions mentioned above. The cells were passaged using PBS and trypsin. All cell lines obtained from NCCS were authenticated by STR profile analysis. Cell lines were tested to be negative for mycoplasma contamination.

A549, HT-29, HCT-116, L929, HEK-293T, MDCK, Vero-E6 and Tb1 Lu cells were obtained from the NCCS cell repository. A549-ACE2 cells were kind gifts from Dr. Shashank Tripathi's lab (Indian Institute of Science).

## METHOD DETAILS

### Protein sequence and structure analysis

CoV-RHIM sequences in coronaviruses, SARS-CoV-2, and other bat RNA viruses were determined based on well-characterized human and viral RHIM protein sequences and amino acid propensities that favor β-sheet amyloid structures. Coronavirus protein sequence alignments were performed using Clustal Omega multiple sequence alignment tool (from EMBL-EBI). Putative RHIM sequences were compared to annotate variation among coronaviruses. Maximum likelihood phylogenetic analysis of protein sequences was done using PhyML 3.1/3.0aLRT in Phylogene.fr, or MEGA-X, and the analysis output was generated in Newick format. Phylogenetic trees were illustrated in MEGA-X (v10.1.7) using PhyML-generated Newick output formats. Crystal structures of Nsp13 (PDB ID: 6ZSL), Apo and RNA-bound forms of Nsp13 (PDB ID: 7CXM), and Nsp14 (PDB ID: 7N0B) of coronaviruses were visualized, and ribbon and surface structure models were prepared using Chimera 1.14 or ChimeraX 1.4 protein model visualization tool.

### Plasmids and constructs

pLVX-EF1alpha-SARS-CoV-2-Nsp13-2xStrep-IRES-Puro, pLVX-EF1alpha-SARS-CoV-Nsp13-2xStrep-IRES-Puro, and pLVX-EF1alpha-MERS-Nsp13-2xStrep-IRES-Puro were a kind gift from Prof. Nevan Krogan's lab (University of California, San Francisco). Nsp13-Tet-mut (residues 193-196, VQIG→AAAA) and Nsp13-Swap-mut (residues 193-196, VQIG→TVLG) constructs were generated by site-directed mutagenesis using overlap extension PCR. The construct expressing Nsp13-EGFP was generated by subcloning the sequence of EGFP from pLVX-EF1alpha-EGFP-2xStrep-IRES-Puro to pLVX-EF1a-SARS-CoV-2-Nsp13-2xStrep-IRES-Puro using overlap extension PCR. Nsp13 domain deletion constructs were generated using overlap extension PCRs in the same vector background of the SARS-CoV-2 Nsp13 expression construct. The coding sequence of human ZBP1 (hZBP1) was amplified from pCMV-Human-ZBP1 cDNA clone expression plasmid (Sino Biological Inc.) and subcloned into pLVX-EF1alpha-2xStrep-IRES-Puro backbone using EcoRI and BamHI restriction sites. ZBP1-RHIM-Mut (residues 205-208, IQIG→AAAA, N211A) was generated by site-directed mutagenesis using overlap extension PCR. The HA-tag sequence was fused at the C-terminus of ZBP1 through PCR primers. The construct expressing hZBP1-dTomato was generated by fusing dTomato coding sequence at the C-terminus of ZBP1 by overlap extension PCR. Other plasmids used in the study, pcDNA3-HA-RIPK3 and pcDNA3-FLAG-RIPK1 were procured from Addgene.

### Cell culture, transfections, and stimulations

For transient expression of proteins, plasmids were transfected into specific cell lines using Xfect (TakaraBio) or Lipofectamine 2000 (Thermo Fisher Scientific) transfection reagents in reduced serum media (Opti-MEM).

For apoptosis and necroptosis activation, HT-29 cells were treated with 30μM Z-VAD(OMe)-FMK (Cayman Chemical) and 500nM SMAC mimetic SM-164 (MedChemExpress). 2 hours after treatment, 100ng/mL recombinant human TNF-α (Abclonal) was added. Tb1 Lu cells were treated with 30μM Z-VAD(OMe)-FMK and 1μM SM-164 2 hours before treatment with 100ng/mL TNF-α. Necroptosis was inhibited in HT29 and Tb1 Lu cells using 5μM MLKL inhibitor – GW806742X (Sigma Aldrich). Influenza A virus (IAV)-infected L929 cells were treated with 30 μM Z-VAD(OMe)-FMK for inducing necroptosis. To activate ZBP1-specific cell death, L929 cells were treated either with a combination of 5ng/mL Leptomycin-B (Sigma-Aldrich) and 100ng/mL IFN-β (Abclonal) or with CBL0137 (Cayman Chemicals). Tb1Lu cells were treated with 5μM CBL0137 alone and in combination with 30 μM Z-VAD.

### IAV infection

Influenza A virus (A/WSN/1933) was generated using 8 plasmid reverse genetics system and propagated in the MDCK cell line to obtain progeny 1 (P1) virus stocks. For IAV infection experiments, cells were seeded in DMEM supplemented with 10% FBS. 24 hours after seeding cells, the media was replaced with DMEM lacking sodium pyruvate (Sigma Aldrich), and cells were infected with IAV. 2 hours post-infection, 10% FBS was added to the cells, and real-time cell death analysis was performed using IncuCyte S3 Live-Cell Analysis instrument (Sartorius).

### Generation of *Zbp1*$^{-/-}$ L929 cells

Lentiviral particles expressing Cas9 were generated by transfecting HEK-293T cells with LentiCas9-Blast, psPAX2, and pMD2.G plasmids using Xfect transfection reagent in Opti-MEM media. Lentiviral supernatants were harvested 48 hours post-transfection. L929 cells were then infected with Cas9-lentiviruses in the presence of polybrene (Sigma-Aldrich) to obtain cells stably expressing Cas9 protein. The cells were selected with Blasticidin (Thermo Fisher Scientific) and maintained in culture. Lentivirus stocks were prepared using transfer plasmid encoding guide-RNA (gRNA) targeting Zbp1 (Sequence: GTCCTTTACCGCCTGAAGA). L929 cells stably expressing Cas9 were infected with Zbp1 gRNA-lentiviruses in the presence of polybrene and selected with Puromycin (Sigma-Aldrich). Loss of ZBP1 protein expression after the selection was confirmed by immunoblotting analysis with anti-ZBP1 antibody.

### Lentivirus-based stable protein expression

To stably express Nsp13 and other domain deletion constructs of Nsp13 in A549, HCT-116, HT-29 and Tb1 Lu cells, lentivirus particles for transducing the cells were generated in HEK293T cells by transfecting Nsp13 expression constructs along with

pCMV-VSVG and psPAX2 plasmids. Lentivirus supernatants were harvested 48 h after transfection, supplemented with an additional 10% FBS and stored at -80°C. The cells were transduced with lentivirus in the presence of 12mg ml-1 of polybrene and subjected to selection with Puromycin.

### SARS-CoV-2 infection and virus titer assays

Constructs expressing SARS-CoV-2 Nsp13-WT, Nsp13-Tet-Mut, Δ1B-Rec1A-Rec2a, Δ1B were transfected in to A549 cells that express ACE2 protein (A549-ACE2). 24 h after transfection, cells were infected with the SARS-CoV-2 virus (Isolate Hong Kong/VM20001061/2020; NR-52282; BEI Resources, NIAID, NIH) at an MOI of 3. Virus inoculum was prepared in DMEM supplemented with 2% FBS and was added to the cells, followed by incubation of the cells for 1 hour at 37°C for allowing virus adsorption onto cells. After 1 h, DMEM containing 2% FBS was added to cells. 48 h after infection, cells were fixed using 4% formaldehyde and subjected to SYTOX green staining for cell death analysis. Whole cell lysates were collected for immunoblotting analysis of SARS-CoV-2 N-protein.

Viral titers were estimated by Vero E6 cell-based plaque assay. At 90% confluency after seeding, cells were incubated at 37°C, with 150 μL of increasing dilutions of virus supernatant collected from SARS-CoV-2 infected A549-ACE2 cells transiently expressing Nsp13-WT, Nsp13-Tet-Mut, Δ1B-Rec1A-Rec2A and Δ1B proteins. The virus inoculum was removed after 1 h and the cells were overlaid with 0.6% Avicel (Dupont, RC-591) prepared in DMEM containing 2% HI-FBS. After 48 h of incubation at 37°C, the cells were fixed with 4% paraformaldehyde. Following fixation, the cells were stained with Crystal Violet (Sigma Aldrich) for 20 minutes, and plaques were visualized.

This study was performed according to the guidelines and in compliance with institutional biosafety guidelines (IBSC/IISc/KS/11/2020; IBSC/IISc/KS/32/2021). SARS-CoV-2 experiments were conducted at viral Biosafety level-3 facility and IAV-WSN experiments were conducted at Biosafety Level-2 facility at Indian Institute of Science (IISc).

### Real time cell death analysis

Real-time cell-death assays were performed using a two-color IncuCyte S3 Live-Cell Analysis instrument (Sartorius). Cell lines were seeded in 12 well plates and treated with cell death-stimulating agents or infected with viruses. Dead cells were stained with 20nM Sytox Green (Thermo Fisher Scientific) a cell-impermeable DNA-binding fluorescent dye which rapidly enters dying cells after membrane permeabilization and fluoresces green. For quantifying cells undergoing apoptosis, 2.5 μM Caspase-3/7 Green Dye (Sartorius) was used. The incucyte Caspase-3/7 dye is a DNA intercalating dye that is activated on cleavage by Caspase3/7. The resulting images and the fluorescence signals were analysed using IncuCyte S3 software, which provides a count for the Sytox or Cleaved Caspase-3/7 Green-positive cells using microscopic images. This data was plotted using GraphPad Prism 9.0 software.

### Pulldown studies for Nsp13-host RHIM interactions

HEK-293T cells were seeded in 100mm dishes and transfected with the constructs expressing WT and mutant forms of Nsp13, ZBP1and RIPK3 for co-immunoprecipitation studies. Depending on the cell death, 27-48 hrs after transfection the cells were lysed in NP-40 lysis buffer (1.0 % NP40, 50mM Tris, pH 8.0, 150mM NaCl supplemented with protease inhibitor and phosphatase inhibitor cocktails), and lysates were cleared by centrifugation at 12000 rpm for 20 min. The cell lysates were incubated with 10 μg of anti-Streptag-Antibody and 2 μg of the indicated primary antibodies for 4–5 h at 4°C. Protein A/G PLUS-Agarose (Santa Cruz Biotechnology) beads were washed with 1XPBS, incubated for 30 min with 3% BSA for blocking, and added to the samples. After 2 h of incubation at 4°C, the agarose beads were then collected by centrifugation at 1000 rpm and washed three times with 1:1 PBS and NP-40 lysis buffer. Immunoprecipitates were eluted from the beads in the sample buffer and subjected to immunoblotting analysis.

The separated insoluble (pellet) fractions were dissolved in NP-40 lysis buffer containing 2% SDS. After solubilization and centrifugation, the supernatant was incubated with antibodies and samples were processed as mentioned for soluble fractions (above).

### Crosslinking of RHIM protein complexes

HEK-293T cells transiently transfected with indicated clones were subjected to lysis with NP-40 lysis buffer (1.0% NP40, 50mM HEPES, pH 8.0, 150mM NaCl with protease inhibitor and phosphatase inhibitor cocktails) containing 2mM Pierce Premium Grade DSP (Thermo Fisher Scientific). Whole cell lysates were collected and incubated at room temperature for 45 min. The reaction was stopped by adding 1M Tris-HCl and incubating for 15 minutes. Whole cell lysates were centrifuged at 10,000 rpm for 15–20 min to separate insoluble fractions (pellet) and soluble fractions. Insoluble fractions (pellets) were washed using lysis buffer and dissolved in NP-40 lysis buffer. Soluble and insoluble lysates were mixed with 4X sample buffer with or without β-mercaptoethanol (BME) and subjected to SDS-PAGE and immunoblotting analysis to monitor the oligomeric status of complexes.

### Immunoblotting analysis

The cells were lysed using NP40-lysis buffer, followed by the addition of sample-loading buffer containing SDS and BME. The lysates were resolved in SDS-PAGE gels (8%, 10% and 12%), and the gels were then subjected to transfer onto PVDF membrane. The membranes were blocked in 5% skimmed milk at room temperature for 1 h and further incubated with primary antibodies overnight at 4°C. The membranes were washed using Tris-buffered saline with tween 20 (TBST), incubated with horseradish peroxidase

(HRP)-conjugated secondary antibodies for 1h at room temperature, and then washed again with TBST. The indicated antibodies were diluted in skimmed milk (primary antibodies: 1:1000; secondary antibodies: 1:5000). Blots were developed using Immobilon Forte Western HRP substrate (Millipore) and visualized using Image Quant LAS500 or Image Quant 800 (Cytiva, Amersham).

### Immunofluorescence and DNA-PAINT imaging

HEK-293T cells were transfected with the respective plasmids (Zbp1-HA, ZBP1-dTomato, ZBP1-RHIM-Mut-HA, RIPK1-FLAG, and RIPK3-HA) along with Nsp13-EGFP. For checking RHIM-dependent interaction, HEK-293T were further transfected with Nsp13-WT and Nsp13-Tet-Mut in combination with RIPK3-HA. 20-22 h after transfection, the cells were fixed with 4% paraformaldehyde in 1X PBS (ChemCruz) for 20 minutes at room temperature. After fixing, cells were permeabilized using 0.1% Triton X-100 for 10 min at room temperature. Nonspecific binding was blocked using 3% BSA (GBiosciences). Cells were incubated with anti-HA Tag or anti-FLAG Tag (Invitrogen) antibody for 1 h at room temperature. The cells were then subjected to staining with Alexa Fluor 568-conjugated anti-mouse IgG (Invitrogen) for 30 mins at room temperature. After each step, the cells were washed twice with 1X PBS. The cells were counterstained with DAPI. All images were acquired using Olympus FV 300 Confocal microscope system. The colocalization analysis was performed using 'Coloc2' plugin of Fiji. The plugin was used to quantify Pearson's correlation coefficient as a mathematical measure of colocalization.

For DNA points accumulation for imaging in nanoscale topography (DNA-PAINT) imaging (ref for protocol), HEK-293T cells were seeded and co-transfected with constructs expressing Nsp13-EGFP along with ZBP1-HA and RIPK3-HA separately. 20-22 h after transfection, the cells were fixed for 15 min using 4% paraformaldehyde (Electron Microscopy Sciences), preheated to 37°C and subjected to 5 washes with PBS, pH 7.4. 1 mg/mL sodium borohydride solution in PBS was used to quench the free aldehyde groups, followed by 5 washes with PBS. The cells were then permeabilized with 0.5% Triton X-100 in PBS for 15 min, followed by 2 washes with PBS. The cells were then incubated with 3 % Bovine Serum Albumin (Sigma, A4503) in PBS for 45 min for blocking, followed by 2 washes with PBS. 1:200 dilution of anti-GFP (Invitrogen, A-11122) and anti-HA tag (Invitrogen, 26183) primary antibodies were prepared in 3 % Bovine Serum Albumin, added to the wells, and incubated overnight in the dark at 4°C followed by 2 washes with PBS. 1:200 dilution of the docking-strand conjugated anti-mouse and anti-rabbit secondary antibody in 3% Bovine Serum Albumin was added to the wells and incubated for 45 minutes at room temperature, followed by 2 washes with PBS. Gold nanoparticles diluted at a 1:5 ratio in PBS was added to the chamber and incubated for 5 min followed by 5 washes with PBS.

Microscopy was performed on a Nikon Ti-2 eclipse microscope equipped with a motorized H-TIRF, perfect focus system (PFS), and a Teledyne Photometrics PRIME BSI sCMOS camera. Illumination using 561 nm wavelength lasers was done using the L6cc Laser combiner from Oxxius Inc., France. Imaging was done under Total Internal Reflection conditions. Imager sequences used for DNA-PAINT were 5'-AGGAGGA-Cy3B-3' and 5'-AGAGAGA-Cy3B-3'. For 2-color imaging of Nsp13-EGFP and RIPK3-HA or ZBP1-HA, the imager solution from the first round of imaging was washed 5 times with buffer C (1× PBS and 500 mM NaCl) with 2 min of incubation. The second imager solution was prepared in buffer C, added to the wells, and imaged at the same plane. For all DNA-PAINT imaging rounds, the laser power was set at 313W/cm2 on the imaging plane, and the image acquisition rate was set to 10 Hz in HiLo mode. The obtained raw fluorescence data was reconstructed using 'Localize' tool embedded in the Picasso Software suite to obtain a super-resolved image (Schnitzbauer et al., 2017). Drift correction was performed by redundant cross-correlation (RCC) followed by correction with fiducial markers. RCC was also used to align the super-resolved structures from the two imaging channels. Reconstructed data was rendered in Picasso:Render. For 2-color data, reconstructed files for both rounds of imaging were individually drift-corrected and loaded into 'Render' together using RCC or gold nanoparticles to align the two images.

### Purification of ZBP1- Zα1Zα2 domain

The bacterial codon-optimized coding sequence of ZBP1- Zα1Zα2 domains was synthesized (Thermo Fisher Scientific) and subcloned into N terminally His-Tagged pNIC-ZB vector. The plasmid expressing pNIC-ZB-ZBP1-Zα1Zα2 was transformed into Rosetta DE3 (kind gift from Prof. B Gopal from MBU, IISc) and grown overnight on LB agar plates with kanamycin and chloramphenicol. Single colonies from the plate were inoculated 20mL LB media and incubated overnight at 37°C at 180 rpm. 20mL overnight cultures were inoculated into 1000 mL of LB containing kanamycin and chloramphenicol. Cultures were grown at 37°C, induced at 0.6 OD (600nm) by adding 0.3 mM IPTG, then incubated for 4 h at 37°C. The pellet lysed in the lysis buffer 50 mM HEPES (pH 7.5), 500 mM NaCl, 5 % glycerol, 1 mM PMSF,1 mM DTT and 5 mM imidazole). Cells were disrupted by subsequent sonication until a clear solution was obtained. The cells were further centrifuged at 18300g for 40 min at 4°C. Ni-NTA beads (Gbioscieces) were loaded on a gravity flow column and washed with 50 ml of lysis buffer containing 10 mM imidazole and a further wash with 25 ml of buffer containing 1M NaCl. Proteins were then eluted with gradient elution (10 mM Tris HCl, 500 mM NaCl, 5% glycerol, 1 mM PMSF, and no imidazole to 500 mM imidazole). The eluted protein was run on a 15% SDS-PAGE gel to check the purity. The eluted protein fraction was further treated with TEV protease to exclude the Z-basic part from the purified protein. Dialysis was performed for the eluted product with 20 mM Tris 7.5, 50 mM NaCl, 2 mM DTT overnight at 4°C. The eluted fraction was passed through the Heparin column. The column was washed with 50 ml of 50 mM HEPES (pH 7.5), 50 mM NaCl, 5% glycerol, 1 mM PMSF. The eluted fractions were pooled and diluted in no salt buffer (50 mM HEPES (pH 7.5), 5 % glycerol,1 mM PMSF). These fractions were further loaded onto the Resource-S cation exchange column (Cytiva, 17117801), which was equilibrated with start buffer (20 mM HEPES pH 7.5 and 50 mM NaCl). The bound protein was eluted using gradient elution buffer (50 mM to 1 M NaCl).

The eluted fractions were run on SDS-PAGE to check the purity of the protein (MW ~22.8 kDa), and the fractions that have pure proteins were pooled, snap frozen, and stored at -80°C.

### SARS-CoV-2 zRNA predictions

The SARS-CoV-2 Wuhan-Hu-1 RNA genome (NCBI, NC_045512.2) was used for predicting the possible Z-RNA forming sequences. Alternative purine-pyrimidine (Pu:Py) repeats and short interspersed nuclear elements (SINEs) with inverted repeats favor RNAs to attain Z-conformation (Balasubramaniyam et al., 2018; Hall et al., 1984; Herbert et al., 2021; Jiao et al., 2020; Thamann et al., 1981; Zhang et al., 2020; Zhang et al., 2022). SARS-CoV-2 genome was assessed for the presence of Pu:Py repeats and SINE-like sequences using Microsatellite repeat finder, the non-B DNA Motif Search Tool (nBMST) and RNAfold developed by Mathew's lab for predicting the secondary structures of RNAs (Cer et al., 2013; Reuter and Mathews, 2010). In the Microsatellite repeat finder, the parameters were extended to inverted repeats, tandem repeats, and Z-DNA-like sequences for identifying Z-RNA-like features. The repeat sequence length was set to a maximum 6 bases, as previous studies established that the Z-nucleic acid sequences are repeats of Pu:Py with a maximum length of 6 (Hall et al., 1984; Placido et al., 2007; Popenda et al., 2004; Thamann et al., 1981). Further, the alternative Pu:Py repeats spanning inverted repeats in the SARS-CoV-2 genome were selected, and the secondary structure was predicted using RNAfold. The nBMST was executed to delineate the sequences forming alternative conformations that differ from the canonical right-handed Watson-Crick double-helix. By utilizing the tool, we predicted sequences with inverted short tandem repeats that form slipped/hairpin-like structures and Z-DNA-like motif sequences with repeats of purines and pyrimidines. The secondary structure of all the possible inverted repeats in the SARS-CoV-2 genome identified as mentioned above was predicted using RNAfold server to illustrate the canonical base pairs that RNA can attain considering free energy minima. The secondary structure of the SARS-CoV-2 genome in infected cells has been solved recently (Huston et al., 2021; Lan et al., 2022; Sun et al., 2021). Using this experimentally solved complete SARS-CoV-2 genome as a reference, we compared the secondary structures of predicted Z-RNA favoring inverted repeats with the experimentally solved secondary structure and precise base pairing events of the SARS-CoV-2 genome. Following the annotations, the SARS-CoV-2 RNA genome segments with Z-RNA forming potential were selected that retain secondary structures and base pairing like experimentally solved structures.

### Probing SC2-zRNA and Zα1Zα2 association using EMSA

To perform EMSAs, SARS-CoV-2 Z-RNA (SC2-zRNA) fragments were generated using *in vitro* transcription method. The HiScribe T7 High Yield RNA Synthesis Kit (NEB, E2040S) was used to transcribe the template DNA per the manufacturer's instructions. The SARS-CoV-2 RNA fragments with Z-RNA forming potential were synthesized as DNA oligos with an upstream T7 promoter sequence (GGATCCTAATACGACTCACTATA). To synthesize uncapped RNA, 1 μg of DNA containing the T7 promoter upstream was mixed with the provided reaction buffer and the DNA oligos complementary to the T7 promoter. The mixture was subjected to a thermal cycling step at 95°C for 5 min. Following the thermal cycling, NTPs (provided in the kit) for RNA synthesis were added to the reaction mixture. The specific NTPs and their concentrations are typically included in the HiScribe T7 High Yield RNA Synthesis Kit. The reaction mixture containing the DNA template, reaction buffer, NTPs, and T7 RNA polymerase was then incubated at 37°C for 14-16 h. This extended incubation period allows the T7 RNA polymerase from the kit to catalyze the transcription process, resulting in the synthesis of uncapped RNA. The purified ZBP1- Zα1Zα2 domain was incubated at different concentrations with different SC2-zRNAs for 30 min at 23°C in the RNA binding buffer (10 mM HEPES pH 7.5, 50 mM NaCl). The RNA-protein mixture was then loaded onto the 6% Native PAGE gel and was run in Tris-boric acid-EDTA (TBE) buffer at 120 V for 40 min at 4°C. Once electrophoresis was completed, the gels were post-stained with ethidium bromide and imaged in the Bio-Print VILBER imaging system.

### SC2-zRNA transfections

24 h after seeding, L929 cells were transfected with the construct expressing Nsp13-WT. 20 h after transfection, the cells were transfected with specified RNAs. 5 μg of RNA (poly I:C, Positive control Z-RNA, indicated SARS-CoV-2 Z-RNAs) was incubated with Lipofectamine 2000 transfection reagent (Invitrogen), for 15 mins at room temperature. After incubation, the transfection mix was added to the cells in Opti-MEM, and cells were subjected to real-time cell death analysis using Sytox Green staining in Incucyte.

### Biolayer interferometry (BLI)-Octet

The binding kinetics of ZBP1- Zα1Zα2 with SARS-CoV-2 RNAs were evaluated using the Octet RED96 instrument (Sartorius). First, amine-reactive second-generation (AR2G) biosensors were equilibrated in a buffer PBS pH 7.4. Then, the AR2G biosensor channel was activated using EDC and sulfo-NHS reagents (Sigma). Following this, ZBP1- Zα1Zα2 was diluted to a concentration of 10 μg/mL and immobilized on activated AR2G biosensors for 300 sec in a 10 mM sodium acetate buffer, pH 4.0. The reaction was quenched by utilizing an excess of sulfo-NHS esters in 1 M ethanolamine. For monitoring SC2-zRNAs interaction with ZBP1- Zα1Zα2, black 96-well plates (Nunc F96 Microwell, Thermo Fisher Scientific) were loaded with 200 μL of the protein or the buffer, maintained at 25°C, and agitated at 1000 rpm. The baseline for each read was recorded using the buffer alone. The association of ZBP1-Zα1Zα2with SC2-zRNAs at 100 nM and 200 nM concentration was captured for 300 sec, followed by the dissociation for 200 sec by dipping the sensor into the buffer without protein. After each kinetic assay, the biosensor chip was regenerated using 0.1 M Glycine-HCl. The acquired kinetic data was analyzed using the manufacturer's software (Data Analysis HT v11.1). A global fitting approach was employed to analyze the data, to fit specific sensograms with a 1:1 binding model.

### Protein-protein and protein-RNA docking studies

The Nsp13 structures (PDB: 7CXM) and the RIPK3-RHIM motif (PDB: 6JPD) were extracted from the Protein Data Bank. We adopted to protein-protein docking to generate the Nsp13-RHIM complexes using High Ambiguity Driven biomolecular DOCKing with default protocol and parameters.[98,99] The Molecular Dynamics (MD) simulation was initiated using the GROMACS-2024.1 software suite compiled with a CUDA dependency on Nvidia RTX GPU machines. Periodic boundary conditions were defined to be cubic with its dimensions expanding around the complex system ensuring 10 Å of space on each side of the 3D box solvated with TIP3P water model. Parameterization was done according to the Charmm36 all-atom force field and under physiological conditions with a pH of 7.0, the MD simulations were carried out.[100] Monte Carlo ion-placement was adopted to neutralize the system with appropriate number of $K^+$ and $Cl^-$ ions in order to ensure that the residues are in their expected ionization states. A force constant of 1,000 kJ/mol·nm2 was consistently applied to restrict the movement of heavy atoms and maintain the native protein folding. Overall MD protocol involved three main stages, the system was initially minimized using the steepest descent algorithm for 5,000 iterations over 5 picoseconds. Following that, a two-step equilibration procedure was carried out, with each stage requiring 100,000 (100 ps) of conditioning rounds. A constant NVT ensemble was used in the first equilibration phase to regulate the temperature, volume, and number of particles. The Berendsen temperature coupling method was used to control the temperature. The Parrinello-Rahman barostat was used in an NPT ensemble during the second equilibration step to keep the temperature, pressure, and particle count constant. The temperature was kept at 303.15 K and the pressure was adjusted to 1 atm. Protein-RNA docking was performed using HDOCK for monitoring SARS-CoV-2 Z-RNA binding to Nsp13.[101]

## QUANTIFICATION AND STATISTICAL ANALYSIS

Statistical significance was determined by two-way ANOVA, one-way ANOVA or T-test using GraphPad Prism software. All analysis was performed for a minimum of $n$=3. P values for each statistical analysis can be found at the end of respective figure legends.